

AD-A180 610

AFWAL-TR-86-3022

DTIC FILE COPY



# BOUNDARY-LAYER STABILITY ANALYSIS FOR SHARP CONES AT ZERO ANGLE-OF-ATTACK

LESLIE M. MACK

JET PROPULSION LABORATORY  
4800 Oak Grove Drive  
Pasadena, California 91109

August 1986

FINAL REPORT FOR PERIOD JUNE 1982-FEBRUARY 1986

MAY 27 1987

A

APPROVED FOR PUBLIC RELEASE: DISTRIBUTION UNLIMITED

FLIGHT DYNAMICS LABORATORY  
AIR FORCE WRIGHT AERONAUTICAL LABORATORIES  
AIR FORCE SYSTEMS COMMAND  
WRIGHT-PATTERSON AIR FORCE BASE, OHIO 45433-6553

87

NOTICE

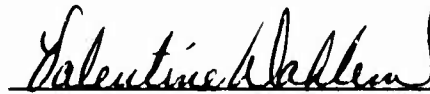
When Government drawings, specifications, or other data are used for any purpose other than in connection with a definitely related Government procurement operation, the United States Government thereby incurs no responsibility nor any obligation whatsoever; and the fact that the government may have formulated, furnished, or in any way supplied the said drawings, specifications, or other data, is not to be regarded by implication or otherwise as in any manner licensing the holder or any other person or corporation, or conveying any rights or permission to manufacture use, or sell any patented invention that may in any way be related thereto.

This report has been reviewed by the Office of Public Affairs (ASD/PA) and is releasable to the National Technical Information Service (NTIS). At NTIS, it will be available to the general public, including foreign nations.

This technical report has been reviewed and is approved for publication.



KENNETH F. STETSON  
Aerospace Engineer  
High Speed Aero Per. Branch  
Aeromechanics Division



VALENTINE DAHLEM, Chief  
High Speed Aero Perf. Branch  
Aeromechanics Division

FOR THE COMMANDER



DONALD A. DREESBACH, Colonel, USAF  
Chief, Aeromechanics Division  
Flight Dynamics Laboratory

"If your address has changed, if you wish to be removed from our mailing list, or if the addressee is no longer employed by your organization please notify AFWAL/FIMG, W-PAFB, OH 45433 to help us maintain a current mailing list".

Copies of this report should not be returned unless return is required by security considerations, contractual obligations, or notice on a specific document.

Unclassified

SECURITY CLASSIFICATION OF THIS PAGE

HD-H 10 610

## REPORT DOCUMENTATION PAGE

1a. REPORT SECURITY CLASSIFICATION Unclassified			1b. RESTRICTIVE MARKINGS		
2a. SECURITY CLASSIFICATION AUTHORITY			3. DISTRIBUTION/AVAILABILITY OF REPORT Approved for public release; distribution unlimited		
2b. DECLASSIFICATION/DOWNGRADING SCHEDULE					
4. PERFORMING ORGANIZATION REPORT NUMBER(S)			5. MONITORING ORGANIZATION REPORT NUMBER(S) AFWAL-TR-86-3022		
6a. NAME OF PERFORMING ORGANIZATION Jet Propulsion Laboratory		6b. OFFICE SYMBOL (If applicable)		7a. NAME OF MONITORING ORGANIZATION Flight Dynamics Laboratory (AFWAL/FIMG)	
6c. ADDRESS (City, State and ZIP Code) 4800 Oak Grove Drive Pasadena, CA 91109			7b. ADDRESS (City, State and ZIP Code) Air Force Wright Aeronautical Laboratories Wright-Patterson AFB, OH 45433-8553		
8a. NAME OF FUNDING/SPONSORING ORGANIZATION		8b. OFFICE SYMBOL (If applicable)		9. PROCUREMENT INSTRUMENT IDENTIFICATION NUMBER NAS7-918, RD-182, A216	
8c. ADDRESS (City, State and ZIP Code)			10. SOURCE OF FUNDING NOS.		
			PROGRAM ELEMENT NO. 61102F	PROJECT NO. 2307	TASK NO. N4
					WORK UNIT NO. 53
11. TITLE (Include Security Classification) Boundary-Layer Stability Analysis for Sharp Cones at Zero Angle-of-Attack (U)					
12. PERSONAL AUTHOR(S) Mack, Leslie M.					
13a. TYPE OF REPORT Final Report		13b. TIME COVERED FROM 6/82 TO 2/86		14. DATE OF REPORT (Yr., Mo., Day) 1986/August	
				15. PAGE COUNT 54	
16. SUPPLEMENTARY NOTATION					
17. COSATI CODES			18. SUBJECT TERMS (Continue on reverse if necessary and identify by block number)		
FIELD	GROUP	SUB GR			
20	04		Boundary layer stability; Hypersonic linear stability theory; Hypersonic cone stability.		
19. ABSTRACT (Continue on reverse if necessary and identify by block number)					
<p>The stability characteristics of an uncooled sharp cone at zero angle of attack have been calculated at an edge Mach number of 6.8 and a stagnation temperature of 728°K (1310°R) using spatial normal modes. Transformed flat-plate boundary-layer profiles were used for the mean flow. By a consideration of both two-dimensional and oblique waves, it has been determined that instability at this Mach number is primarily a two-dimensional second-mode instability. Comparisons with available stability experiments show that the calculated unstable frequencies were present in the experiments, but the measured amplification rates differ from the calculated. A band of unstable high frequencies above the second-mode region that starts at about <math>R=1400</math> is not accounted for by the theory. Comparisons of amplitude-growth curves for both cones and flat plates at Mach numbers 4.5, 5.8 and 6.8 show that the most unstable normal modes on a cone have a least as much total growth as on a flat plate at Mach 4.5, and more total growth at the other two Mach numbers.</p>					
20. DISTRIBUTION/AVAILABILITY OF ABSTRACT UNCLASSIFIED/UNLIMITED <input checked="" type="checkbox"/> SAME AS RPT <input type="checkbox"/> DTIC USERS <input type="checkbox"/>			21. ABSTRACT SECURITY CLASSIFICATION Unclassified		
22a. NAME OF RESPONSIBLE INDIVIDUAL Kenneth F. Stetson			22b. TELEPHONE NUMBER (Include Area Code) (513) 255-5419		22c. OFFICE SYMBOL AFWAL/FIMG

## FOREWORD

This document presents the results of an investigation into the stability of uncooled cone boundary layers at hypersonic speeds. The work described in the report was carried out at the Jet Propulsion Laboratory, California Institute of Technology, under contract NAS7-913, RD-182, A-216 with the National Aeronautics and Space Administration (NASA), pursuant to AFWAL MIPR Nos. FY1456-82-N0021, FY1456-83-N0001, and FY1456-84-N0006. This report is the final report for Work Unit 2307N453.



A-1

## TABLE OF CONTENTS

SECTION		PAGE
I	INTRODUCTION	1
II	COMPRESSIBLE STABILITY EQUATIONS	3
III	CONE STABILITY EXPERIMENTS	7
IV	NUMERICAL PROCEDURES	8
	1. Mean Boundary Layer	8
	2. Stability Calculations	8
V	NUMERICAL RESULTS	11
	1. Results at $M_e = 6.8$	11
	2. Comparisons with Experiment	23
	3. Cone vs Flat Plate	32
VI	CONCLUDING REMARKS	36
	APPENDIX	38
	REFERENCES	41

# LIST OF FIGURES

Figure	Page
1 Multiple 2D temporal eigenvalues vs wavenumber at $R = 9000$ : $M_e = 6.8$ , cone; $T_0^* = 512^\circ K$ ( $922^\circ R$ ). . . . .	10
2 Multiple 2D spatial eigenvalues vs wavenumber at $R = 1732$ . $M_e = 6.8$ , cone; $T_0^* = 728^\circ K$ ( $1310^\circ R$ ). . . . .	12
3 Effect of stagnation temperature on 2D spatial amplification rate vs frequency at $R = 1732$ . $M_e = 6.8$ , cone. . . . .	14
4 Spatial amplification rate vs Reynolds number for several frequencies; 2D waves. $M_e = 6.8$ , cone; $T_0^* = 728^\circ K$ ( $1310^\circ R$ ). . . . .	15
5 Phase velocity vs Reynolds number for three frequencies; 2D waves. $M_e = 6.8$ , cone; $T_0^* = 728^\circ K$ ( $1310^\circ R$ ). . . . .	16
6 $N$ factor vs Reynolds number for several frequencies and envelope curve; 2D waves. $M_e = 6.8$ , cone; $T_0^* = 728^\circ K$ ( $1310^\circ R$ ). . . . .	16
7 Neutral boundaries, locus of maximum spatial amplification rate and locus of maximum amplitude ratio; 2D waves. $M_e = 6.8$ , cone; $T_0^* = 728^\circ K$ ( $1310^\circ R$ ). . . . .	18
8 Effect of wave angle on spatial amplification rate of three frequencies at $R = 1245$ . $M_e = 6.8$ , cone; $T_0^* = 728^\circ K$ ( $1310^\circ R$ ). . . . .	19
9 Effect of wave angle on spatial amplification rate of three frequencies at $R = 1732$ . $M_e = 6.8$ , cone; $T_0^* = 728^\circ K$ ( $1310^\circ R$ ). . . . .	20
10 Maximum spatial amplification rate vs frequency at $R = 1245$ ; wave angle noted where different from zero. $M_e = 6.8$ , cone; $T_0^* = 728^\circ K$ ( $1310^\circ R$ ). . . . .	21
11 Wave angle vs Reynolds number for four oblique waves; $F = 1.0 \times 10^{-4}$ $M_e = 6.8$ , cone; $T_0^* = 728^\circ K$ ( $1310^\circ R$ ). . . . .	22
12 Spatial amplification rate vs Reynolds number for four oblique waves and comparison with 2D wave; $F = 1.0 \times 10^{-4}$ : $M_e = 6.8$ , cone; $T_0^* = 728^\circ K$ ( $1310^\circ R$ ). . . . .	23
13 $N$ factor vs Reynolds number for four oblique waves and comparison with 2D wave; $F = 1.0 \times 10^{-4}$ . $M_e = 6.8$ , cone; $T_0^* = 728^\circ K$ ( $1310^\circ R$ ). . . . .	24
14 Spatial amplification rate vs frequency at $R = 1731$ . Comparison of calculated maximum with respect to $\beta$ with experimental points from Ref. 16. $M_e = 6.8$ , cone; $T_0^* = 728^\circ K$ ( $1310^\circ R$ ). . . . .	25
15 Experimental spatial amplification rate vs Reynolds number for three frequencies from Ref. 16. $M_e = 6.8$ , cone; $T_0^* = 728^\circ K$ ( $1310^\circ R$ ). . . . .	26
16 Comparison of calculated maximum 2D spatial amplification rate vs Reynolds number with experimental values from Ref. 16. $M_e = 6.8$ , cone; $T_0^* = 728^\circ K$ ( $1310^\circ R$ ). . . . .	27
17 Comparison of calculated frequency of maximum 2D spatial amplification rate with experimental values from Ref. 16. $M_e = 6.8$ , cone; $T_0^* = 728^\circ K$ ( $1310^\circ R$ ). . . . .	28
18 Comparison of calculated 2D $N$ factor vs Reynolds number with faired amplitude-growth curve from Ref. 16. $M_e = 6.8$ , cone; $F = 1.2 \times 10^{-4}$ , $T_0^* = 728^\circ K$ ( $1310^\circ R$ ). . . . .	28

## LIST OF FIGURES (concluded)

Figure	Page
19 Comparison of calculated 2D $N$ -factor envelope curve with experimental peak amplitudes from Ref. 18. $M_e = 6.8$ , cone; $T_0^* = 728^\circ K$ ( $1310^\circ R$ ). . . . .	29
20 Comparison of calculated 2D envelope-curve frequencies of peak amplitude from Ref. 16. $M_e = 6.8$ , cone; $T_0^* = 728^\circ K$ ( $1310^\circ R$ ). . . . .	30
21 Calculated neutral boundaries and boundary between first and second mode; measured upper and lower limits of first spectral bump from Ref. 16, $M_e = 6.8$ , cone; $T_0^* = 728^\circ K$ ( $1310^\circ R$ ). . . . .	31
22 Comparison of 2D cone and flat-plate $N$ -factor envelope curves. $M_e = 4.5$ , $T_0^* = 311^\circ K$ ( $560^\circ R$ ). . . . .	32
23 Comparison of 2D cone $N$ -factor envelope curve with curves of $N$ factor vs Reynolds number for three flat-plate oblique waves with $\psi = 55^\circ$ at critical Reynolds number. $M_e = 4.5$ , $T_0^* = 311^\circ K$ ( $560^\circ R$ ). . . . .	33
24 Comparison of 2D cone $N$ -factor envelope curve with curves of $N$ factor vs Reynolds number for two oblique waves on a cone with $\beta R = 201.7$ . $M_e = 4.5$ , $T_0^* = 311^\circ K$ ( $560^\circ R$ ). . . . .	34
25 Comparison of 2D cone and flat-plate $N$ -factor envelope curves. $M_e = 5.8$ , $T_0^* = 386^\circ K$ ( $696^\circ R$ ). . . . .	34
26 Comparison of 2D cone and flat-plate $N$ -factor envelope curves. $M_e = 6.8$ , $T_0^* = 728^\circ K$ ( $1310^\circ R$ ). . . . .	35

## NOMENCLATURE

$A$	In theory, integral of spatial amplification rate; In experiment, narrow-band rms disturbance amplitude
$A_0$	Reference $A$ in $N$ -factor calculation; value of $A$ at $R_0$
$A_1$	Reference $A$ in experimental $N$ factor
$A_{maz}$	Measured $A$ at peak of first spectral bump
$D$	$d/dy$
$F$	Dimensionless frequency ( $= \omega^* \nu^* / U_e^{*2}$ )
$L^*$	Reference length, Eq. (15)
$M$	Mach number
$N$	$N$ factor, Eq. (17)
$Re$	$x$ -Reynolds number
$R$	Reference Reynolds number, Eq. (16)
$R_0$	Lower-branch neutral $R$ of given $F$
$S_u, S_d$	Families of eigensolutions
$T$	Temperature
$T_0$	Freestream stagnation temperature
$U$	Mean velocity
$U_e^*$	Reference velocity
$Z_i$	Dependent variables defined by Eq. (12)
$a_{ij}$	Coefficient matrix of stability equations (see Appendix)
$c$	Phase velocity
$c_p$	Specific heat
$d$	$\lambda/\mu$
$f$	Frequency
$p$	Pressure fluctuation
$r$	Density fluctuation
$u, v, w$	Fluctuation velocity components
$x$	Coordinate in flow direction
$y$	Coordinate normal to wall
$z$	Spanwise (azimuthal) coordinate



## NOMENCLATURE (concluded)

$\alpha, \beta$	Complex wavenumber components
$\alpha_{1n}$	Multiple wavenumbers at which $c = 1.0$
$\gamma$	Ratio of specific heats
$\theta$	Temperature fluctuation
$\kappa$	Thermal conductivity coefficient
$\lambda$	Second viscosity coefficient
$\lambda$	Wavelength
$\mu$	Viscosity coefficient
$\nu$	Kinematic viscosity coefficient
$\rho$	Mean density
$\sigma$	Prandtl number ( $= c_p^* \mu^* / \kappa^*$ )
$\sigma$	Spatial amplification rate ( $= -\alpha_i$ )
$\sigma_{maz}$	Maximum $\sigma$ with respect to spanwise wavenumber
$\psi$	Wave angle
$\omega$	Circular frequency
$\omega_i$	Temporal amplification rate

## SUPERSCRIPTS

*	Dimensional quantity
'	Refers to fluctuation in $\kappa$ , $\lambda$ , or $\mu$

## SUBSCRIPTS

$e$	Boundary-layer edge condition
$0$	Initial reference condition
$\delta$	Refers to boundary-layer thickness ( $U = 0.999$ )
$\infty$	Undisturbed freestream

## OTHER

—	Total flow quantity
$\wedge$	Eigenfunction

STDS Reference 16

## SECTION I INTRODUCTION

The stability theory of compressible boundary layers has been largely developed on the basis of numerical calculations made for flat-plate boundary layers (see e.g., Mack, Refs. 1 and 2). Even with the simplification of a zero pressure gradient, the dependence on Mach number and the ratio of surface temperature to recovery temperature introduces enough complexity to bring out a wide range of physical phenomena that have no counterparts in low-speed stability theory. The stability of sharp-cone boundary layers at zero angle-of-attack has been commonly supposed to be closely related to flat-plate stability, but except for a series of calculations by Malik (Ref. 3) at supersonic Mach numbers, the numerical consequences of the difference in geometry have not been extensively investigated.

Because of the simplicity of the geometry, cones were popular test models in early transition experiments. A celebrated flight experiment by Sternberg (Ref. 4) achieved an exceptionally high transition Reynolds number on the nose cone of a V2 rocket. Wind-tunnel transition experiments on sharp cones were carried out by Laufer and Marte (Ref. 5), Van Driest and Boison (Ref. 6), Potter and Whitfield (Ref. 7) and Pate (Ref. 8), among others. In addition, a "standard" cone was tested in a large number of transonic wind tunnels and the transition Reynolds number was used as a calibration device for the disturbance level in the tunnels, (Dougherty and Steinle, Ref. 9). The same cone was later used in a significant flight test (Dougherty and Fisher, Ref. 10). A cone was also the model of choice in ballistic-range experiments, (Potter, Ref. 11; Sheetz, Ref. 12; Reda, Ref. 13).

Transition experiments, where nothing is measured except a transition Reynolds number, are difficult to relate directly to stability theory, although a consistently calculated  $N$  factor has been shown by Malik (Ref. 3) to be useful as a correlation device. Stability experiments, where disturbance growth is measured in the boundary layer prior to transition, offer better possibilities of relating theory to experiment. The only cone stability experiments are those of Kendall (Ref. 14), of Demetriades (Ref. 15), and of Stetson, Thompson, Donaldson and Siler (Refs. 16, 17, 18). These experiments are discussed in Section III, and numerical comparisons between stability calculations and the sharp-cone measurements of Stetson *et al.* (Ref. 16) are given in Section V.2.

Transition on blunt cones has been investigated by Brinich and Sands (Ref. 19), Stetson and Rushton (Ref. 20), Stainback (Ref. 21), Softley (Ref. 22), Muir and Trujillo (Ref. 23) and Stetson (Ref. 24). All of these experiments are in accord that small bluntness increases the transition Reynolds number, but that large bluntness decreases it. The only stability experiment on the effect of cone bluntness has been carried out by Stetson *et al.* (Ref. 17). A theoretical work on bluntness effects has been carried out by Khan and Reshotko (Ref. 25) for a flat plate.

Transition on cones is believed to be caused by boundary-layer instability in much the same way as on flat plates, and the explanation of the effects of bluntness should therefore lie within the scope of stability theory. Any such demonstration is critically dependent on having an exact calculation of the flow over the blunted cone, and this requirement has so far precluded the application of stability theory to this problem. However, no specific demonstration of the applicability of stability theory to transition on a cone has been given even for the simple case of a sharp cone at zero angle-of-attack. The mean boundary layer in

this case can be obtained by the Mangler transformation from the flat-plate boundary layer if the boundary-layer thickness is considered to be negligible with respect to the cone radius. The result is that the cone boundary layer at a given  $x$ -Reynolds number  $Re$  is identical to the flat-plate boundary layer at  $Re/3$ . The consequences of using this transformation for the mean flow together with the planar stability equations were worked out by Battin and Lin (Ref. 26) for two-dimensional (2D) waves. Although the critical Reynolds number of a given frequency on the cone is three times that on the flat plate, the cone amplitude ratio  $A/A_0$  is equal to the cube of the flat-plate amplitude ratio at the same boundary-layer thickness. This result concerning the critical Reynolds numbers led originally to the unwarranted conclusion that the transition Reynolds number on a cone should be three times that on a flat plate. A modification by Tetervin (Ref. 27) gave the result that the ratio should be three only at low transition Reynolds numbers, and should decrease to unity at high transition Reynolds numbers. No actual stability calculations directed to the cone-flat plate comparison have been published, although it is apparent that because of the faster growth on a cone there must be instances where the amplitude ratio on a cone is greater than on a flat plate at the same Reynolds number.

The experimental evidence on the ratio of cone to flat-plate transition Reynolds numbers is confusing. Comparisons of experimental data on cones and on flat plates and hollow cylinders (considered to be equivalent to a flat plate) have been made by Potter and Whitfield (Ref. 7), Whitfield and Ianuzzi (Ref. 28) and Pate (Ref. 8). The extensive comparison by Pate of all available experiments showed, in agreement with Potter and Whitfield and with Whitfield and Ianuzzi, that the ratio is about 2.5 at  $M_\infty = 3$  and decreases steadily to 1 at hypersonic Mach numbers, in general agreement with Tetervin. All authors compared what is essentially the end-of-transition Reynolds numbers. However, Laufer and Marte (Ref. 5) measured transition on a  $2.5^\circ$  half-angle cone in two wind tunnels, and compared the results with flat-plate transition measurements in one of the wind tunnels at similar unit Reynolds numbers between  $M_\infty = 2$  and 5. The comparison showed the end-of-transition Reynolds numbers, in the authors words, to be "not very different." The reason for this difference with the conclusions of Refs. 7 and 28 is that the flat-plate transition Reynolds numbers of Laufer and Marte were much higher than the flat-plate and hollow-cylinder transition Reynolds numbers of the other investigators at low Mach numbers.

The original aim of the present work was to investigate the hypersonic stability characteristics of both sharp and blunt cones with normal-mode stability calculations based on conventional linear stability theory. The mean flow over blunt cones was to have been obtained from the AFWAL state-of-the-art parabolized Navier-Stokes code. However, the viscous shock-layer profiles produced by this code were found to not be of the quality required in a stability analysis. Therefore, this report is restricted to a study of the stability of sharp-cone boundary layers at zero angle-of-attack. Standard linear stability theory is used to carry out a thorough numerical study of normal-mode stability characteristics on a cone with special reference to the conditions of the Stetson *et al.* (Ref. 16) stability experiment (referred to hereafter as STDS). In Section V.2 comparisons of the calculations with experimental measurements bring out major areas of disagreement which remain to be resolved even in this supposedly simple case. In addition, a series of calculations in Section V.3 of both cone and flat-plate  $N$  factors at three Mach numbers show what one might expect the relation between transition on a cone and a flat plate to be on the basis of stability theory.

## SECTION II

### COMPRESSIBLE STABILITY EQUATIONS

The same compressible stability equations will be used as in planar flow. The coordinate system is Cartesian with the  $x^*$  axis along the cone surface in the flow direction, the  $y^*$  axis normal to the surface, and the  $z^*$  axis in the spanwise (azimuthal) direction. All quantities with asterisks are dimensional. The derivation starts with the Navier-Stokes equations for a perfect gas. The flow quantities, denoted by an overbar, are divided into a mean flow and an unsteady term.

$$\begin{aligned}(\bar{u}^*, \bar{v}^*, \bar{w}^*) &= (U^*, V^*, W^*) + (u^*, v^*, w^*), \quad \bar{p}^* = P^* + p^*, \\ \bar{T}^* &= T^* + \theta^*, \quad \bar{\rho}^* = \rho^* + r^*, \\ \bar{\mu}^* &= \mu^* + \mu'^*, \quad \bar{\kappa}^* = \kappa^* + \kappa'^*, \quad \bar{\lambda}^* = \lambda^* + \lambda'^*.\end{aligned}\tag{1}$$

These quantities are, respectively, the velocity components, pressure, temperature, density, viscosity coefficient, thermal conductivity coefficient and second viscosity coefficient. The first term on each RHS is the steady mean-flow term; the second is an unsteady fluctuation. The latter are denoted by lower-case letters except for the transport terms, where a prime is used. The equations are linearized with respect to the fluctuations, the mean-flow terms subtracted out, and, finally, the assumption of locally parallel, or quasiparallel, flow is made. The resulting equations are made dimensionless with respect to the local freestream, or boundary-layer edge, velocity  $U_e^*$ , a reference length  $L^*$ , and the edge values of all state variables including the pressure. Both viscosity coefficients are referred to  $\mu_e^*$  and  $\kappa^*$  is referred to  $c_p^* U_e^*$ , where  $c_p^*$  is the specific heat at constant pressure. The transport coefficients are functions only of temperature, so that their fluctuations can be written

$$\mu' = (d\mu/dT)\theta, \quad \kappa' = (d\kappa/dT)\theta, \quad \lambda' = (d\lambda/dT)\theta.\tag{2}$$

Therefore,  $\mu$ ,  $\kappa$  and  $\lambda$  in the following equations, along with  $\rho$ , are mean-flow quantities, not fluctuations.

The dimensionless, linearized  $x$ -momentum equation is

$$\begin{aligned}\rho \left( \frac{\partial u}{\partial t} + U \frac{\partial u}{\partial x} + v \frac{\partial U}{\partial y} + W \frac{\partial U}{\partial z} \right) &= \frac{1}{\gamma M_e^2} \frac{\partial p}{\partial x} \\ &+ \frac{1}{R} \left[ 2\mu \frac{\partial^2 u}{\partial x^2} + \mu \left( \frac{\partial^2 u}{\partial y^2} + \frac{\partial^2 u}{\partial z^2} + \frac{\partial^2 v}{\partial x \partial y} + \frac{\partial^2 w}{\partial x \partial z} \right) \right. \\ &+ \frac{2}{3}(\lambda - \mu) \left( \frac{\partial^2 u}{\partial x^2} + \frac{\partial^2 v}{\partial x \partial y} + \frac{\partial^2 w}{\partial x \partial z} \right) + \frac{d\mu}{dt} \frac{dT}{dy} \left( \frac{\partial u}{\partial y} + \frac{\partial v}{\partial x} \right) \\ &\left. + \frac{d\mu}{dT} \left( \frac{d^2 U}{dy^2} \theta + \frac{dU}{dy} \frac{\partial \theta}{\partial y} \right) + \frac{d^2 \mu}{dT^2} \frac{dT}{dy} \frac{dU}{dy} \theta \right].\end{aligned}\tag{3}$$

The y-momentum equation is

$$\begin{aligned}
\rho \left( \frac{\partial v}{\partial t} + U \frac{\partial v}{\partial x} + W \frac{\partial v}{\partial z} \right) = & -\frac{1}{\gamma M_e^2} \frac{\partial p}{\partial y} \\
& + \frac{1}{R} \left[ 2\mu \frac{\partial^2 v}{\partial y^2} + \mu \left( \frac{\partial^2 v}{\partial x^2} + \frac{\partial^2 v}{\partial z^2} + \frac{\partial^2 u}{\partial x \partial y} + \frac{\partial^2 w}{\partial y \partial z} \right) \right. \\
& + \frac{2}{3}(\lambda - \mu) \left( \frac{\partial^2 u}{\partial x \partial y} + \frac{\partial^2 v}{\partial y^2} + \frac{\partial^2 w}{\partial y \partial z} \right) + \frac{d\mu}{dT} \left( 2 \frac{dT}{dy} \frac{\partial v}{\partial y} + \frac{dU}{dy} \frac{\partial \theta}{\partial x} + \frac{dW}{dy} \frac{\partial \theta}{\partial z} \right) \\
& \left. + \frac{2}{3} \left( \frac{d\lambda}{dT} - \frac{d\mu}{dT} \right) \frac{dT}{dy} \left( \frac{\partial u}{\partial x} + \frac{\partial v}{\partial y} + \frac{\partial w}{\partial z} \right) \right].
\end{aligned} \tag{4}$$

The z-momentum equation is

$$\begin{aligned}
\rho \left( \frac{\partial w}{\partial t} + U \frac{\partial w}{\partial x} + v \frac{dw}{dy} + W \frac{\partial w}{\partial z} \right) = & -\frac{1}{\gamma M_e^2} \frac{\partial p}{\partial z} \\
& + \frac{1}{R} \left[ 2\mu \frac{\partial^2 w}{\partial z^2} + \mu \left( \frac{\partial^2 w}{\partial y^2} + \frac{\partial^2 w}{\partial x^2} + \frac{\partial^2 v}{\partial y \partial z} + \frac{\partial^2 u}{\partial x \partial z} \right) \right. \\
& + \frac{2}{3}(\lambda - \mu) \left( \frac{\partial^2 w}{\partial z^2} + \frac{\partial^2 v}{\partial y \partial z} + \frac{\partial^2 u}{\partial x \partial z} \right) + \frac{d\mu}{dT} \frac{dT}{dy} \left( \frac{\partial w}{\partial y} + \frac{\partial v}{\partial z} \right) \\
& \left. + \frac{d\mu}{dT} \left( \frac{d^2 W}{dy^2} \theta + \frac{dW}{dy} \frac{\partial \theta}{\partial y} \right) + \frac{d^2 \mu}{dT^2} \frac{dT}{dy} \frac{dW}{dy} \theta \right].
\end{aligned} \tag{5}$$

The continuity equation is

$$\frac{\partial r}{\partial t} + \rho \left( \frac{\partial u}{\partial x} + \frac{\partial v}{\partial y} + \frac{\partial w}{\partial z} \right) + v \frac{d\rho}{dy} + U \frac{\partial r}{\partial x} + W \frac{\partial r}{\partial z} = 0. \tag{6}$$

The energy equation is

$$\begin{aligned}
\rho \left( \frac{\partial \theta}{\partial t} + U \frac{\partial \theta}{\partial x} + v \frac{dT}{dy} + W \frac{\partial \theta}{\partial z} \right) = & -(\gamma - 1) \left( \frac{\partial u}{\partial x} + \frac{\partial v}{\partial y} + \frac{\partial w}{\partial z} \right) \\
& + \left( \frac{\gamma \mu}{\sigma R} \right) \left[ \frac{\partial^2 \theta}{\partial x^2} + \frac{\partial^2 \theta}{\partial y^2} + \frac{\partial^2 \theta}{\partial z^2} + \frac{1}{\kappa} \frac{d\kappa}{dT} \frac{d^2 T}{dy^2} \theta + \frac{2}{\kappa} \frac{d\kappa}{dT} \frac{dT}{dy} \frac{\partial \theta}{\partial y} \right. \\
& + \frac{1}{\kappa} \frac{d^2 \kappa}{dT^2} \left( \frac{dT}{dy} \right)^2 \theta \left. \right] + \gamma(\gamma - 1) M_e^2 \frac{1}{R} \left[ 2\mu \frac{dU}{dy} \left( \frac{\partial u}{\partial y} + \frac{\partial v}{\partial x} \right) \right. \\
& \left. + 2\mu \frac{dW}{dy} \left( \frac{\partial v}{\partial z} + \frac{\partial w}{\partial y} \right) + \frac{d\mu}{dT} \left( \frac{dU}{dy} \right)^2 \theta + \frac{d\mu}{dT} \left( \frac{dW}{dy} \right)^2 \theta \right].
\end{aligned} \tag{7}$$

The equation of state is

$$p = r/\rho + \theta/T. \quad (8)$$

Other quantities that appear in these equations are  $M_e$ , the local edge Mach number;  $R = U_e^* L^* / \nu_e^*$ , the reference Reynolds number;  $\gamma$ , the ratio of specific heats; and  $\sigma = c_p^* \mu^* / \kappa^*$ , the Prandtl number, which is a function of temperature. These equations are valid for a three-dimensional (3D) disturbance in a 3D mean flow.

The boundary conditions at  $y = 0$  are

$$u(0) = 0, v(0) = 0, w(0) = 0, \theta(0) = 0. \quad (9)$$

The temperature-fluctuation condition is suitable for a gas flowing over a solid wall. The boundary conditions at  $y \rightarrow \infty$  are

$$u(y), v(y), w(y), \rho(y), \theta(y) \text{ bounded as } y \rightarrow \infty. \quad (10)$$

The solutions to these equations are specialized to

$$[u, v, w, p, r, \theta]^T = [\hat{u}(y), \hat{v}(y), \hat{w}(y), \hat{p}(y), \hat{r}(y), \hat{\theta}(y)]^T \exp \left[ i \left( \int^x \alpha dx + \beta z - \omega t \right) \right], \quad (11)$$

where  $\alpha$  and  $\beta$  are the wavenumber components, and  $\omega$  is the frequency. These solutions are locally normal modes, but are also suitable for a mean flow that is varying with  $x$  and constant in  $z$  and  $t$ . For a constant frequency, Eq. (11) represents a spatial wave train.

When the individual components of Eq. (11) are substituted into Eqs. (3)–(8), a system of ordinary differential equations is obtained for  $\hat{u}(y)$ , etc. These equations are not yet in a form that is suitable for numerical computation. With the dependent variables defined by

$$Z_1 = \alpha \hat{u} + \beta \hat{w}, Z_2 = DZ_1, Z_3 = \hat{v}, Z_4 = \hat{p}/\gamma M_e^2, Z_5 = \hat{\theta}, \quad (12)$$

$$Z_6 = D\hat{\theta}, Z_7 = \alpha \hat{w} - \beta \hat{u}, Z_8 = DZ_7,$$

where  $D = d/dy$ , the equations can be written as eight first-order differential equations

$$DZ_i(y) = \sum_{j=1}^8 a_{ij}(y) Z_j(y), \quad (i = 1, 8). \quad (13)$$

The lengthy equations for the coefficient matrix elements  $a_{ij}$  are listed in the Appendix. The boundary conditions are

$$Z_1(0) = 0, Z_3(0) = 0, Z_5(0) = 0, Z_7(0) = 0, \quad (14)$$

$$Z_1(y), Z_3(y), Z_5(y), Z_7(y) \text{ bounded as } y \rightarrow \infty.$$

Equations (13) plus the boundary conditions, Eq. (14), constitute an eigenvalue problem for the wave parameters  $\alpha$ ,  $\beta$  and  $\omega$ . In general all of these parameters are complex. Two of the six real parameters can be determined as eigenvalues; the other four must be specified in some way. There is a different eigenvalue relation to solve for each value of the Reynolds number, even when the boundary layer is self-similar. For the spatial waves used in this report, the frequency is real and specified, and the spanwise (azimuthal) wavenumber component  $\beta$  is also real and specified. The way it is specified is discussed in Section V.1 in connection with Fig.10. With  $\beta$  and  $\omega$  known, the complex wavenumber component  $\alpha = \alpha_r + i\alpha_i$  is determined as an eigenvalue by a Newton-Raphson local search procedure. The real part,  $\alpha_r$ , is the streamwise wavenumber component, and the negative of the imaginary part,  $-\alpha_i$ , is the spatial amplification rate.

With the spatial amplification rate known, it can be integrated with respect to  $x$  for a constant frequency to give the  $N$  factor. With the length scale defined to be

$$L^* = (\nu_e^* x^* / U_e^*)^{1/2}, \quad (15)$$

the reference Reynolds number is

$$R = U_e^* L^* / \nu_e^* = (U_e^* x^* / \nu_e^*)^{1/2}, \quad (16)$$

which is just the square root of the usual  $x$ -Reynolds number. The  $N$  factor can be written in terms of  $R$  for a zero pressure-gradient boundary layer as

$$N = \ln(A/A_0) = -2 \int_{R_0}^R \alpha_i dR, \quad (17)$$

where  $A$  can be considered an amplitude, and  $A_0$  is the value of  $A$  at the initial Reynolds number  $R_0$ . It is usual, as in this report, to take  $R_0$  to be the critical Reynolds number of the given frequency. For a pressure-gradient or nonsimilar boundary layer, more complicated expressions for  $N$  are needed.

### SECTION III

## CONE STABILITY EXPERIMENTS

The three stability experiments that have been carried out with sharp cones at zero angle of attack are those of Kendall (Ref. 14) at  $M_\infty = 7.7$  and of Demetriades (Ref. 15) and STDS (Stetson *et al.*, Ref. 16) at  $M_\infty = 8.0$ . The latter two experiments are closely related as they were performed in the same wind tunnel and used some of the same equipment and data-reduction techniques. Kendall used a cooled  $4.5^\circ$  half-angle cone with the ratio of surface temperature to recovery temperature equal to 0.6. Demetriades used a  $4^\circ$  cone, both cooled and uncooled, and STDS an uncooled  $7^\circ$  cone. Reference 15 also includes some results from an earlier experiment with an uncooled  $5^\circ$  cone. There is some disagreement in detail among the experiments, but general agreement that at a fixed Reynolds number there is a band of unstable frequencies with the lower frequencies being only weakly amplified and the higher frequencies more strongly amplified with a marked peak in amplification rate that is closer to the upper-branch neutral frequency than to the lower-branch neutral frequency. If the disturbances are assumed to be waves moving at phase velocities nearly equal to the edge mean velocity, the wave lengths of the most unstable disturbances are about two boundary-layer thicknesses. This fact identifies the disturbances as two-dimensional second-mode waves. All three experiments gave another band of unstable frequencies starting at a frequency above the upper-branch neutral frequency of the second mode. These unstable frequencies have no counterparts in linear stability theory.

Kendall (Ref. 14) obtained his amplification rates by first finding, at an initial  $x$  station, the  $y$  at which the narrow-band response for a selected frequency was a maximum. This position is well defined near the edge of a hypersonic boundary layer where there is a generalized inflection point. The hot-wire probe was then traversed downstream at the  $y/y_\delta$  of maximum response, subject to occasional checks to see if the response was still a maximum, and with an appropriate adjustment in position if it was not. The slope of the amplitude vs  $x$  curve that resulted gave the spatial amplification rate.

The experimental amplification rates of Demetriades (Ref. 15) and STDS (Ref. 16) were obtained from power spectra as measured by a hot wire (STDS) or hot film (Demetriades). A spectrum was measured at one  $x$  station, then the hot wire was moved to another station and a second spectrum measured. At each  $x$ , the hot wire or film was placed at the  $y$  position of maximum wide-band response. The sequence of amplitudes for a given frequency determined the spatial amplification rate. Thus at each frequency, any shift of spectral amplitude from one  $x$ -station to the next is interpreted to be a result of instability; an amplitude increase is amplification; a decrease is damping. This procedure ignores the possibility that the spectrum in certain frequency ranges may change from other influences than instability, such as receptivity. Also, unlike Kendall's experiment, no allowance was made for the fact that different frequencies may have their peak responses at different  $y/y_\delta$ .

The experiment of STDS will be used for all experimental comparisons because of the detail of the published measurements. The measurements that will be used are not raw hot-wire data, but the results of computerized data procedures. In addition to the discussion of these procedures and the data included in the original paper (Ref. 16), the appendices of Ref. 18, particularly Appendices A and D, give a further discussion of the data and their interpretation which applies to the sharp-cone experiment at zero angle-of-attack, and several figures in Ref. 18 give the results of a reassessment of some of the Ref. 16 data.



## SECTION IV NUMERICAL PROCEDURES

### 1. MEAN BOUNDARY LAYER

The boundary layer on a sharp cone at zero angle of attack in supersonic flow can be obtained from a flat-plate boundary layer at the same edge Mach number by the simple transformation mentioned in the Introduction, which is a special case of the general Mangler (Ref. 29) transformation for axisymmetric bodies. The transformation states that on a cone the boundary layer at  $3Re$  is identical to a flat-plate boundary layer at  $Re$ . This transformation is valid where there is no interaction between the shock wave and the boundary layer. Even so, it ignores the effect of transverse curvature, which is important whenever the boundary-layer thickness is not negligible compared to the cone radius.

Two computer programs were used to produce the boundary-layer profiles used in the stability calculations. The first, BL-1, developed by the author, uses a Jet Propulsion Laboratory (JPL) variable-step, variable-order Adams-Moulton integration subroutine to solve the exact zero pressure-gradient planar compressible boundary-layer equations for a perfect gas. The viscosity and thermal conductivity coefficients have exactly the same form as in the stability equations [see Appendix, Eqs. (A11) and (A12)]. There is an option for a constant Prandtl number that is used when it is necessary to make stability calculations to compare with other authors. The code produces tables of  $U, DU, D^2U, T, DT, D^2T$  which can be read directly by the input subroutines of the stability codes.

The second program, BL-2, is based on the boundary-layer portion of the TAPS code (Gentry and Wazzan, Ref. 30). This is basically a finite-difference Cebeci-Smith code (Ref. 31) and can be applied to incompressible (water and air) and compressible boundary layers on planar surfaces, including infinite-span swept wings, and on axisymmetric bodies. For the latter, an option allows the transverse curvature effect to be included. The I/O subroutines and the subroutine that calculates the thermodynamic properties were completely rewritten to be compatible with the program BL-1. A feature of code BL-2 is that self-similar solutions may also be produced, which allows a direct check to be made against results obtained with BL-1.

### 2. STABILITY CALCULATIONS

The stability codes used in this investigation are descendants of the 2D temporal viscous code described by Mack (Ref. 32). This code was extended to 3D temporal waves by use of the Squire transformation, and then largely rewritten in single-precision complex arithmetic in about 1970 to allow spatial, temporal and spatial/temporal calculations to be carried out. The complex Squire transformation was used for 3D spatial waves and Gram-Schmidt orthonormalization adopted to remove the limitation to low Reynolds numbers. The code underwent another significant change in 1977 when the complex Squire transformation was abandoned as the method of treating 3D waves and 3D boundary layers in favor of the system of equations given in the Appendix. During this same period the original Adams-Moulton integrator was replaced by a Runge-Kutta integrator, subroutines were added to allow the automatic calculation of large numbers of eigenvalues in a single computer run, the capability to analyze nonsimilar boundary layers was added, and the I/O portions of the

code were rewritten to enable the code to be operated conveniently in a time-sharing rather than a batch environment.

Although code development was not an objective of the present contract, much time had to be devoted to this type of work in order to be able to carry out the large number of stability calculations that were required. The original plan to use the AFWAL computer for most of the stability calculations as well as the mean-flow calculations, had to be abandoned because no satisfactory communications link was available. Therefore, the calculations that were done during the original period of performance of this contract used the JPL Univac 1100/81 computer, where the cost is based largely on the product of the program size in main memory and residence time. To reduce this cost, a simplified version (called SFREQ) of the current JPL code was developed for a single frequency. The new code contained numerous improvements, which were then incorporated into an extensively revised version of the complete code, called BLS. Most of the numerical results given in this report were obtained from code BLS. Even with all of this programming effort, difficulties were still encountered in carrying out the eigenvalue calculations, and these difficulties are mentioned in Section V.

Finally, in the course of preparing this report a Hewlett-Packard 9000, Series 500, Model 550, 32-bit dual-processor super-microcomputer became available at no cost. A number of additional numerical calculations, which could not be made on the Univac because of cost considerations, were made with this facility. The three-megabyte memory of this computer allowed storage arrays to be enlarged, and because the computation time was no longer a major consideration, more use could be made of double-precision arithmetic in the critical parts of the calculation, and finer integration meshes and additional iterations could also be used. Also the user interface was greatly simplified and made more convenient by taking advantage of the UNIX operating system of the new computer. The porting of the codes SFREQ and BLS to the new computer, and the writing of the new interface, were done under NASA sponsorship.

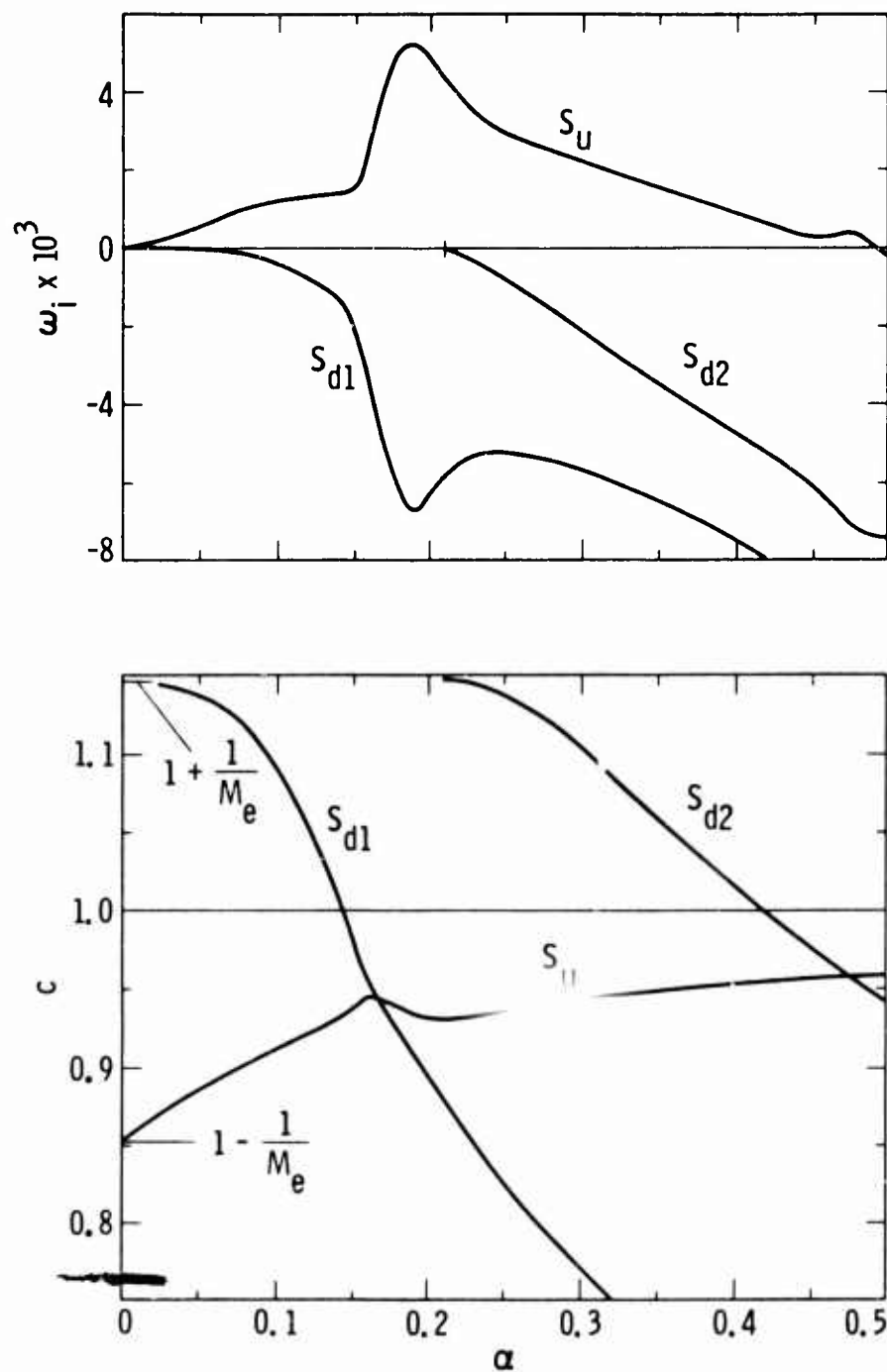


Figure 1. Multiple 2D temporal eigenvalues vs wavenumber at  $R = 9000$ : temporal amplification rate (top); phase velocity (bottom).  $M_e = 6.8$ , cone;  $T_0^* = 512^\circ K$  ( $922^\circ R$ ).

## SECTION V

### NUMERICAL RESULTS

The numerical results in this Section are divided into three parts. In Part 1, results are given at  $M_e = 6.8$  for the Reynolds number range of the experiment of STDS. In Part 2, comparisons are made with the measurements of STDS. In Part 3, calculations that cover a wider range of Reynolds numbers are given at  $M_e = 4.5, 5.8,$  and  $6.8$  for both cones and flat plates.

#### 1. RESULTS AT $M_e = 6.8$

There is no large body of hypersonic cone stability calculations as there is for a flat plate (Mack, Refs. 1 and 2). To remedy this lack, extensive calculations of normal-mode stability characteristics have been carried out in cone variables at the edge Mach number of STDS. All of the calculations are for an insulated-wall boundary layer. Three different methods were used to obtain the necessary mean-flow boundary layers. The first method used the transformed flat-plate profiles calculated from either code BL-1 or BL-2. This method has the advantage that the profiles are self-similar and the results depend only on the edge Mach number and stagnation temperature, not on the cone angle. In the second method, code BL-2 was used to calculate self-similar cone profiles from the axisymmetric boundary-layer equations for a cone without the transverse curvature term. Calculations made with these profiles served as a check that the transformation was done correctly in the first method. Lastly, the transverse-curvature effect was included in the axisymmetric equations, and the nonsimilar boundary layer calculated from code BL-2. The latter calculation, where the cone angle is a parameter, was restricted to the STDS half angle of  $7^\circ$ .

To properly carry out the eigenvalue calculations, and to understand a major numerical difficulty that was encountered, it is necessary to have some information about the different families of eigensolutions that exist for hypersonic boundary layers. For this purpose, it is convenient to start with the temporal theory and the transformed flat-plate boundary layer with a freestream temperature of  $T_e^* = 50^\circ K$  ( $90^\circ R$ ), the same as in the calculations of Mack (Ref. 1). The stagnation temperature is  $T_0^* = 512^\circ K$  ( $922^\circ R$ ). One feature of hypersonic stability calculations with the present numerical method that is quite different from low-speed calculations is that very good guesses of eigenvalues are required for the local search procedure to converge to the least-stable solution. With this choice of a boundary layer and a high Reynolds number, the flat-plate temporal 2D inviscid eigenvalue diagrams of Mack (Ref. 1) at  $M_e = 7.0$  can be used to give the much-needed eigenvalue guesses. The first calculations were carried out at  $R = 9000$ . The temporal amplification rate  $\omega_i$  and the phase velocity  $c$  are given as functions of the wavenumber  $\alpha$  in Fig. 1. Three families of solutions are shown. Family  $S_u$  starts at  $\alpha = 0$ ,  $c = 1 + 1/M_e$  and contains the first-mode, second-mode and third-mode unstable solutions. All three modes are merged into a single unstable region extending from  $\alpha = 0$  to  $\alpha = 0.492$ . The second mode is the most unstable, and the third mode is barely discernible. Family  $S_{d1}$  starts at  $\alpha = 0$ ,  $c = 1 + 1/M_e$  and is composed only of damped solutions. For  $\alpha < \alpha_{11} = 0.142$ , the phase velocity  $c$  is greater than 1, and for  $\alpha > 0.23$  the phase velocity is supersonic with respect to the freestream. Family  $S_{d2}$  starts at  $\alpha = 0.21$ ,  $c = 1 + 1/M_e$  and also consists only of damped solutions. For  $\alpha < \alpha_{12} = 0.417$ ,  $c$  is greater than 1. Note that in the inviscid theory all waves with  $c > 1$  are neutral; here, even at the high Reynolds number of 9000, they are damped.

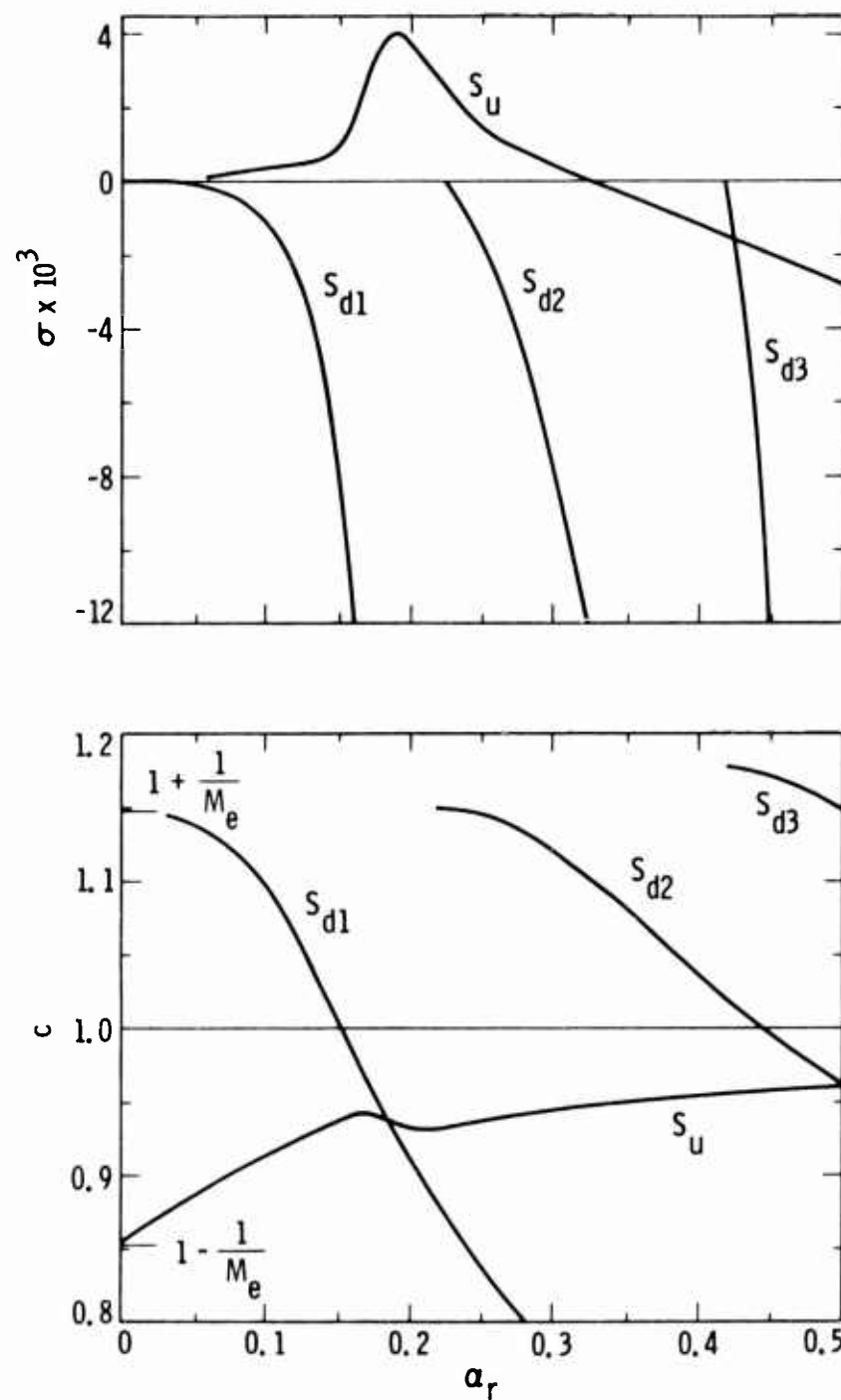


Figure 2. Multiple 2D spatial eigenvalues vs wavenumber at  $R = 1732$ : spatial amplification rate (top); phase velocity (bottom).  $M_e = 6.8$ , cone;  $T_0^* = 728^\circ K$  ( $1310^\circ R$ ).

The eigenvalue diagrams of the multiple spatial solutions are similar to those of the temporal solutions. Also, with the 2D eigenvalues known, the eigenvalues for oblique waves can readily be calculated. The effect of wave obliqueness is to destabilize the first mode, and to stabilize the second and higher modes and move them to higher wavenumbers. The higher modes, and all of the multiple solutions, depend on the existence of a region of flow in the boundary layer that is supersonic with respect to the phase velocity. As the wave angle  $\psi$  increases, this region of relative supersonic flow becomes thinner and vanishes completely at some  $\psi > 0$ . Above this wave angle, there is only a single family of solutions.

With the multiple viscous solutions known at  $R = 9000$ , they can be extended to the lower Reynolds numbers of interest here. Figure 2 gives the results for spatial 2D waves at  $R = 1732$ . The spatial amplification rate  $\sigma (= -\alpha_i)$  is given in the upper part and the phase velocity in the lower part. The stagnation temperature has been increased to  $728^\circ K$  ( $1310^\circ R$ ). The effect of stagnation temperature is discussed immediately below. At this lower Reynolds number, there is a change in the appearance of the amplification diagram. All traces of the third mode have disappeared, and the unstable wave-number extend only to  $\alpha_r = 0.3245$ . A principal effect of the lower Reynolds number is that the damping rates are much larger than at  $R = 9000$ . The phase-velocity diagram still has the same general appearance as at the higher Reynolds number. A fourth solution,  $S_{d3}$ , is shown. This solution is also present at  $R = 9000$ , but was not calculated. Note that at the limiting lower wavenumber of  $S_{d3}$  ( $\alpha_r = 0.420$ ) at  $R = 1732$ , the phase velocity does not approach  $1 + 1/M_e$ , but a value a few percent higher. Indeed, solution  $S_{d2}$  also approaches a value slightly higher than  $1 + 1/M_e$ .

The flat-plate hypersonic boundary-layer calculations of Ref. 1 were all for  $T_e^* = 50^\circ K$  ( $90^\circ R$ ). As the experiments of Demetriades and STDS were with higher temperatures, the sensitivity of the results to the stagnation temperature for an insulated-wall boundary layer must be established. With the assumption of a perfect gas, the temperature enters through the viscosity and thermal-conductivity coefficients. Figure 3 gives the spatial amplification rate of 2D waves as a function of the dimensionless frequency  $F = (\omega^* \nu_e^* / U_e^{*2})$  for two insulated-wall boundary layers with  $T_e^* = 50^\circ K$  ( $90^\circ R$ ) and  $73.3^\circ K$  ( $132^\circ R$ ). The latter temperature corresponds to  $T_0^* = 728^\circ K$  ( $1310^\circ R$ ), which is the freestream stagnation temperature used in most of the measurements of STDS.

Figure 3 shows that increasing the stagnation temperature has a considerable stabilizing influencing at  $M_e = 6.8$ . The amplification rate is lowered at almost all frequencies, and the unstable frequency band is narrowed by about 15%. In view of this large effect, which is particularly pronounced in  $N$ -factor calculations, the subsequent stability calculations will be for the stagnation temperature of  $728^\circ K$  ( $1310^\circ R$ ). There is a further slight stabilization at the highest stagnation temperature of the STDS experiments,  $1350^\circ R$ , but this is not significant.

Some parameters of the self-similar insulated-wall cone boundary layer with  $T_0^* = 728^\circ K$  ( $1310^\circ R$ ) are: wall temperature,  $T_w^* = 609^\circ K$  ( $1096^\circ R$ ); temperature recovery factor, 0.819; dimensionless displacement thickness referenced to  $L^*$ , 11.01; dimensionless momentum thickness, 0.3421; boundary-layer thickness, defined as the  $y$  where  $U = 0.999$ ,  $y_\delta = 13.42$ ; generalized inflection point,  $y_{inf}/y_\delta = 0.876$  ( $U = 0.956$ ); relative sonic point for  $c = 0.956$ ,  $y_s/y_\delta = 0.511$ . Note that  $T_w^*/T_0^* = 0.837$ , which compares well with the measured 0.84 in Ref. 16 at  $x^* = 15.1$  in. from the cone tip.

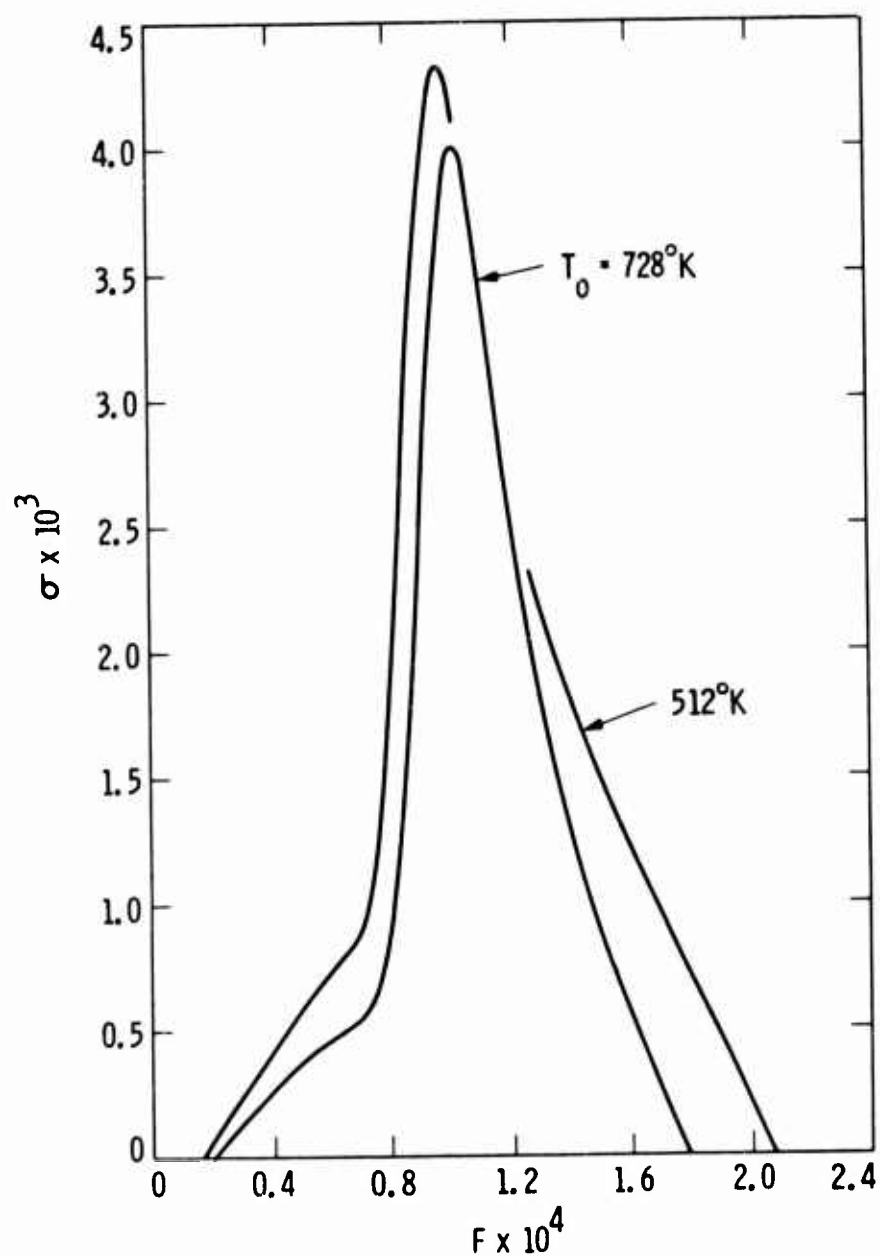


Figure 3. Effect of stagnation temperature on 2D spatial amplification rate vs frequency at  $R = 1732$ .  $M_e = 6.8$ , cone.



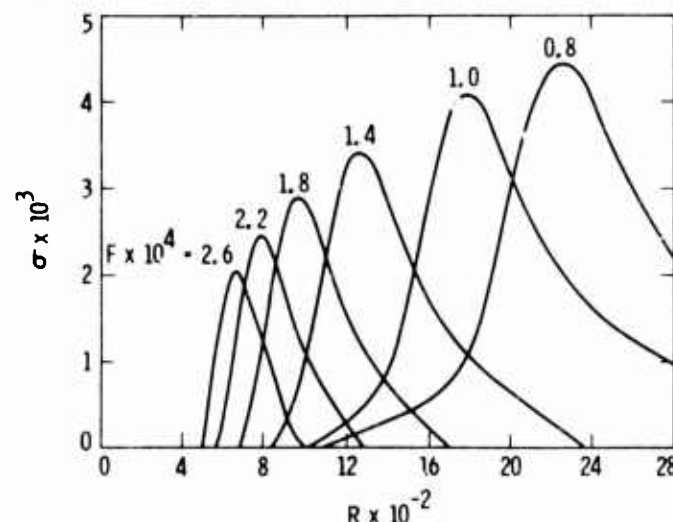


Figure 4. Spatial amplification rate vs Reynolds number for several frequencies; 2D waves.  $M_e = 6.8$ , cone;  $T_0^* = 728^\circ K$  ( $1310^\circ R$ ).

Next, program BL-2 was used to calculate the cone boundary layer with  $T_0^* = 728^\circ K$  ( $1310^\circ R$ ) and the transverse curvature term included for a cone half angle of  $7^\circ$ . This boundary layer is nonsimilar, so that in the stability calculations a different profile must be used at each  $x$  station along the cone. The stability codes are set up for this type of input, and a calculation of the growth of a constant frequency wave as it propagates downstream is carried out in exactly the same way as for a self-similar boundary layer, except that the Reynolds numbers are restricted to those at which profiles are available. A considerable number of calculations were performed with the nonsimilar profiles, and no important differences were found in comparison with the results obtained with the self-similar profiles. For example, including transverse curvature at  $R = 1732$  reduced the amplification rate of a wave with  $F = 1.0 \times 10^{-4}$  from  $3.94 \times 10^{-3}$  to  $3.80 \times 10^{-3}$ , and the  $N$  factor from 1.87 to 1.75. In view of these small differences, all subsequent calculations were performed without the transverse curvature term. This procedure has the advantage that the results are applicable to any cone angle, and also makes the stability equations completely consistent with the boundary-layer equations.

The 2D stability characteristics for the  $M_e = 6.8$  boundary layer without transverse curvature were calculated for several frequencies with the stagnation temperature equal to  $728^\circ K$  ( $1310^\circ R$ ), as it will be in all of the subsequent calculations. The complex wavenumber is obtained as an eigenvalue for the given  $F$  and  $R$  with  $\beta = 0$ . Each value of  $F$  may be considered to represent a single 2D wave that is excited at some upstream location, and at each downstream location corresponds to the 2D normal mode for that particular  $F$  and  $R$ . The spatial amplification rate is given as a function of  $R$  for several frequencies in Fig. 4. The higher frequencies, to the left in the figure, belong completely to the second mode. The two lowest frequencies have a first-mode region, as is apparent from the smaller slope, followed by a second-mode region where the slope increases. A 2D wave can only have appreciable amplification at this Mach number, as at all hypersonic Mach numbers, when it is a second-mode wave. Note that as with all self-similar boundary layers, the maximum amplification



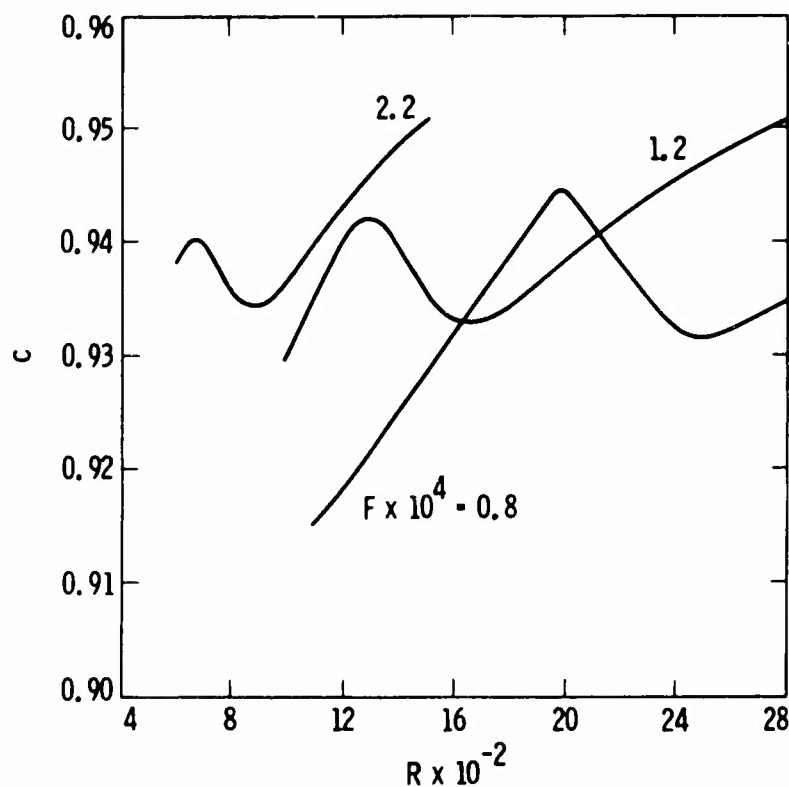


Figure 5. Phase velocity vs Reynolds number for three frequencies; 2D waves.  $M_e = 6.8$ , cone;  $T_0^* = 728^\circ K$  ( $1310^\circ R$ ).

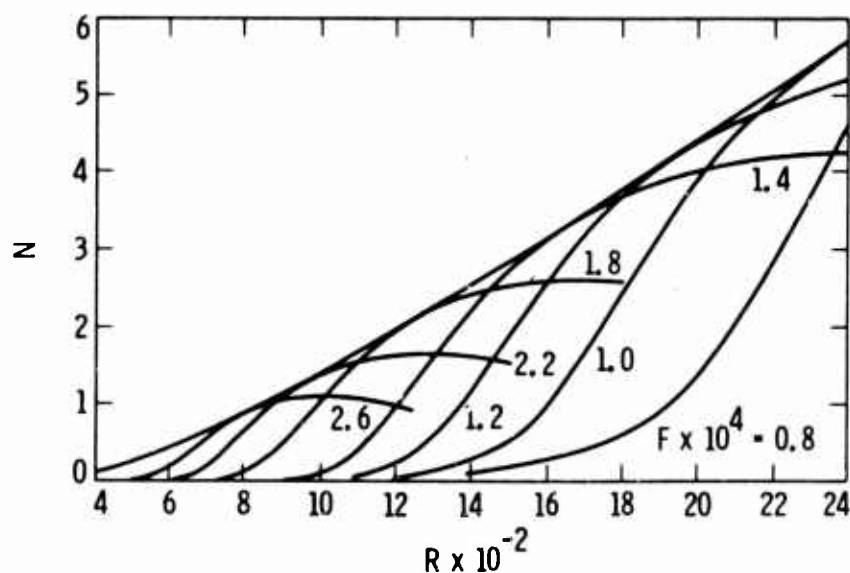


Figure 6.  $N$  factor vs Reynolds number for several frequencies together with envelope curve; 2D waves.  $M_e = 6.8$ , cone;  $T_0^* = 728^\circ K$  ( $1310^\circ R$ ).

rate for each frequency increases monotonically with decreasing frequency.

The phase velocity of three 2D waves is given in Fig. 5 as a function of Reynolds number. The characteristic feature of this figure is that, while phase velocity decreases with increasing  $R$  there is a range of Reynolds numbers for each frequency where the phase velocity decreases with increasing  $R$ . This behavior is characteristic of the second mode, so that it is in these regions that the most unstable waves are located. The maximum amplification rate is located just past the center of each reverse-slope region where  $c$  is approximately 0.936 for each of the three frequencies. Interestingly,  $c$  is not far from this value all along the  $N$ -factor envelope curve. It is 0.935 at  $R = 970$  (where  $F = 2.2 \times 10^{-4}$ ), and increases very slightly with increasing  $R$ .

The  $N$  factors for seven frequencies, as calculated from Eq. (17), are given in Fig. 6 as a function of  $R$ . In this figure, all substantial amplification is second mode in character. The separate curves for  $F \times 10^4 = 0.8$  and 1.0 show clearly the difference between weak first-mode amplification and strong second-mode amplification. In Fig. 6, the envelope curve, which is the maximum value of  $N$  that is possible at any  $R$ , has been drawn graphically. The stability program BLS is provided with an automatic procedure for calculating  $N$ -factor envelope curves that is intended to obviate the need to draw the curve graphically. However, this procedure, which works well in incompressible flow and at low Mach numbers, could not be used because of a numerical difficulty.

This difficulty arises from the small radius of convergence at hypersonic Mach numbers of the eigenvalue search procedure for the least-stable solution. If no convergence at all is obtained at some  $F$  when calculating eigenvalues for the unstable frequency band at a given  $R$ , the code reduces the  $F$  increment until convergence is obtained and the calculation continues. It so happens that at a given  $F$ ,  $R$  the  $S_{dn}$  damped solutions have a much larger radius of convergence, and there is likely to be convergence to one of these solutions. By tracking the phase velocity, the unwanted eigenvalues are disregarded by the program and the  $F$  increment reduced just as when no convergence is obtained. The net effect of the convergence failures and the false convergences was to so increase the amount of computation that the automatic procedure could no longer be used, and the envelope curve had to be drawn graphically.

In Fig. 7, the neutral-stability curves in  $\alpha_r$ ,  $R$  and  $F$ ,  $R$  space are shown for 2D normal modes. Also shown in the figure are two other curves that give the loci of the maximum spatial amplification rate and the  $N$ -factor envelope curve of Fig. 6. It is of interest that at the higher Reynolds numbers the latter two curves are virtually independent of  $R$  in the  $\alpha_r$ ,  $R$  plane. A constant dimensionless  $\alpha_r$  means that the dimensional wavelength  $\lambda^* (= 2\pi L^*/\alpha_r^*)$  is proportional to the boundary-layer thickness. This result is due to the primarily inviscid nature of second-mode instability. The ratio of wavelength to boundary-layer thickness (defined as the  $y$  where  $U = 0.999$ ) is 1.9 on the  $N$ -factor envelope curve at  $R = 2000$ , and this value is characteristic of second-mode waves of maximum growth. The fact that  $c$  is also nearly constant along the envelope curve means that the dimensional frequency scales with the boundary-layer thickness just as does the wavelength.

The previous results are all for 2D waves. Although 2D second-mode normal modes are the most unstable, oblique waves are also unstable and must be looked at. Figure 8 shows the effect of wave angle on the spatial amplification rate of three frequencies at  $R = 1245$ . The actual independent variable of the calculations was the spanwise wavenumber component  $\beta$ , but it is more convenient to plot the results in terms of the angle  $\psi$ . The direction of wave

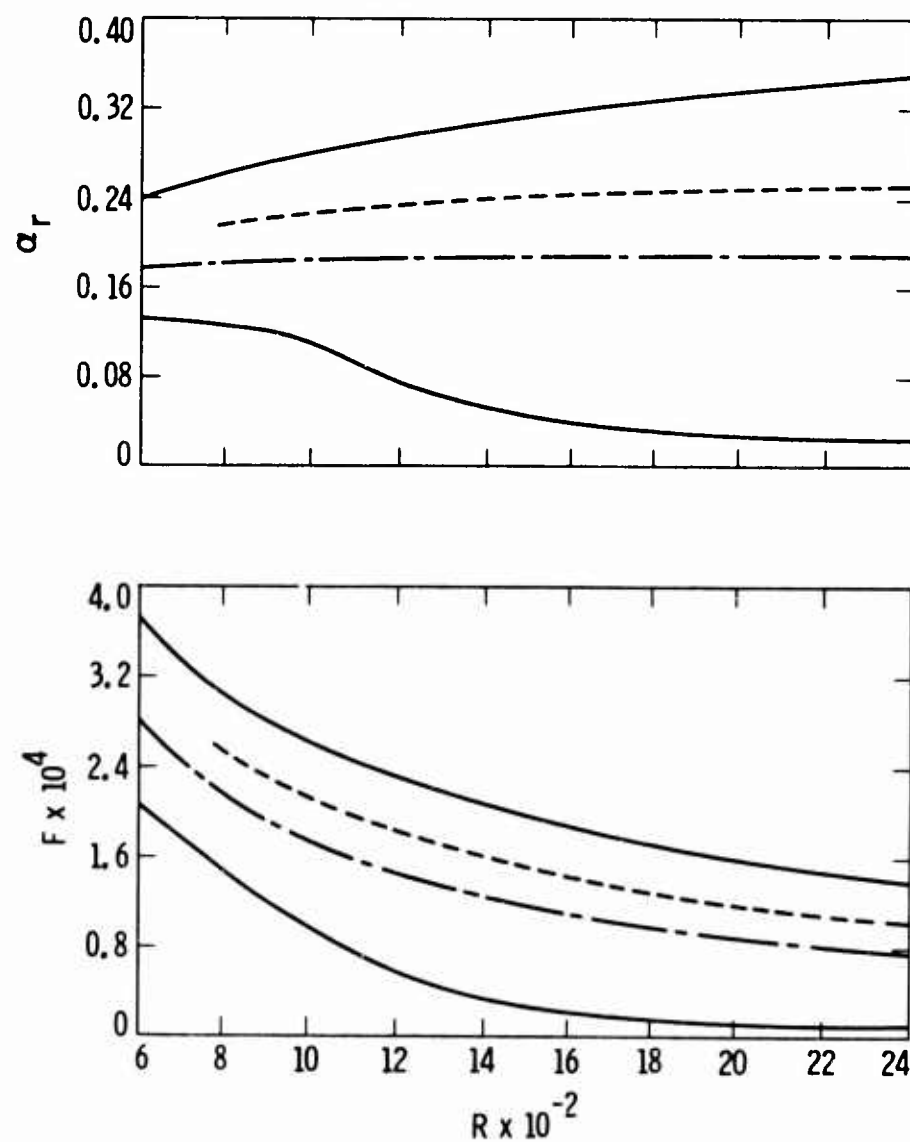


Figure 7. Neutral boundaries, —; locus of maximum spatial amplification rate, — · —; locus of maximum amplitude ratio, - - -; 2D waves: wavenumber vs Reynolds number (top); frequency vs Reynolds number (bottom).  $M_e = 6.8$ , cone;  $T_0^* = 728^\circ K$  ( $1310^\circ R$ ).

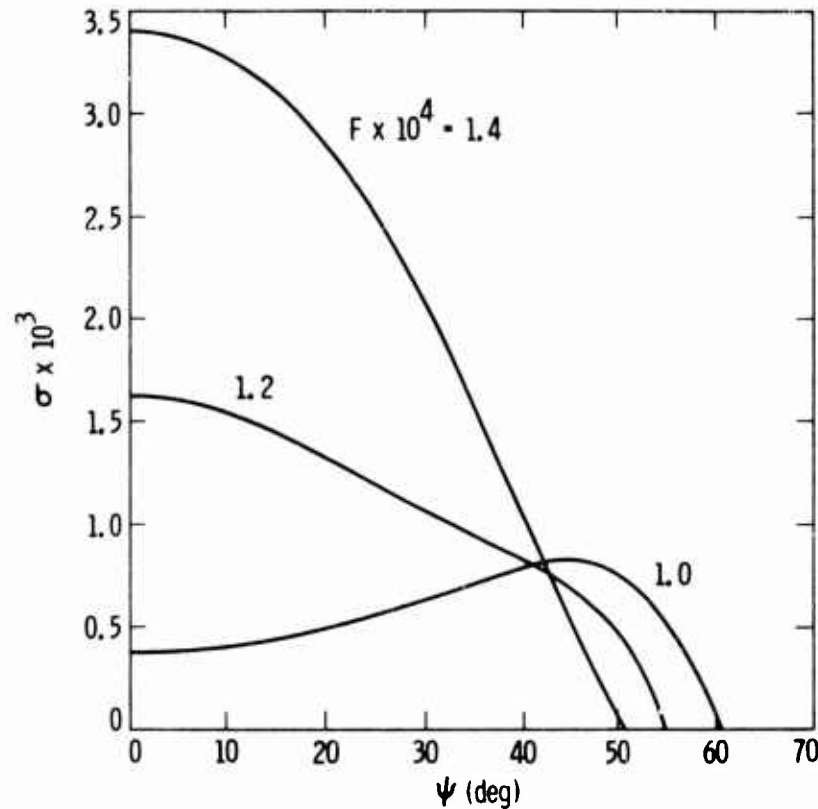


Figure 8. Effect of wave angle on spatial amplification rate of three frequencies at  $R = 1245$ .  $M_e = 6.8$ , cone;  $T_0^* = 728^\circ K$  ( $1310^\circ R$ ).

growth, which is a free parameter for spatial normal modes, has been taken as the freestream direction. This choice is suitable for a 2D boundary layer where the wave-train solution Eq. (11) simulates a physical wave whose initial amplitude is independent of  $z$ . The wave with  $F = 1.4 \times 10^{-4}$  has its maximum amplification rate as a 2D wave, as is characteristic of second-mode behavior. It is only at wave angles near the neutral point that this frequency betrays a hint of first-mode behavior in the existence of an inflection point in the  $\sigma$  vs  $\psi$  curve that moves the neutral point to a slightly higher wave angle than for a pure second-mode wave. At  $F = 1.2 \times 10^{-4}$ , the inflection point has moved to a smaller  $\psi$  and the first-mode character is more pronounced for the larger wave angles. At  $F = 1.0 \times 10^{-4}$ , all of the oblique normal modes, as well as the 2D normal mode, are first mode and the maximum amplification rate occurs at  $\psi = 45^\circ$ .

Figure 9 is similar to Fig. 8 except that it is for  $R = 1732$ . At this higher Reynolds number,  $F = 1.0 \times 10^{-4}$ , which was purely first mode at  $R = 1245$ , is now almost entirely of second-mode character except near the neutral point at  $\psi = 55^\circ$ . The frequency  $F = 0.9 \times 10^{-4}$  has first-mode character for  $\psi$  greater than about  $30^\circ$ , and  $F = 0.7 \times 10^{-4}$  is a first-mode wave at all wave angles. It is apparent from Figs. 8 and 9 that as the Reynolds number increases, lower and lower values of  $F$  take on second-mode character.

Another way to show the demarcation between first and second-mode behavior at a given Reynolds number is to plot the maximum amplification rate, where the maximum is with

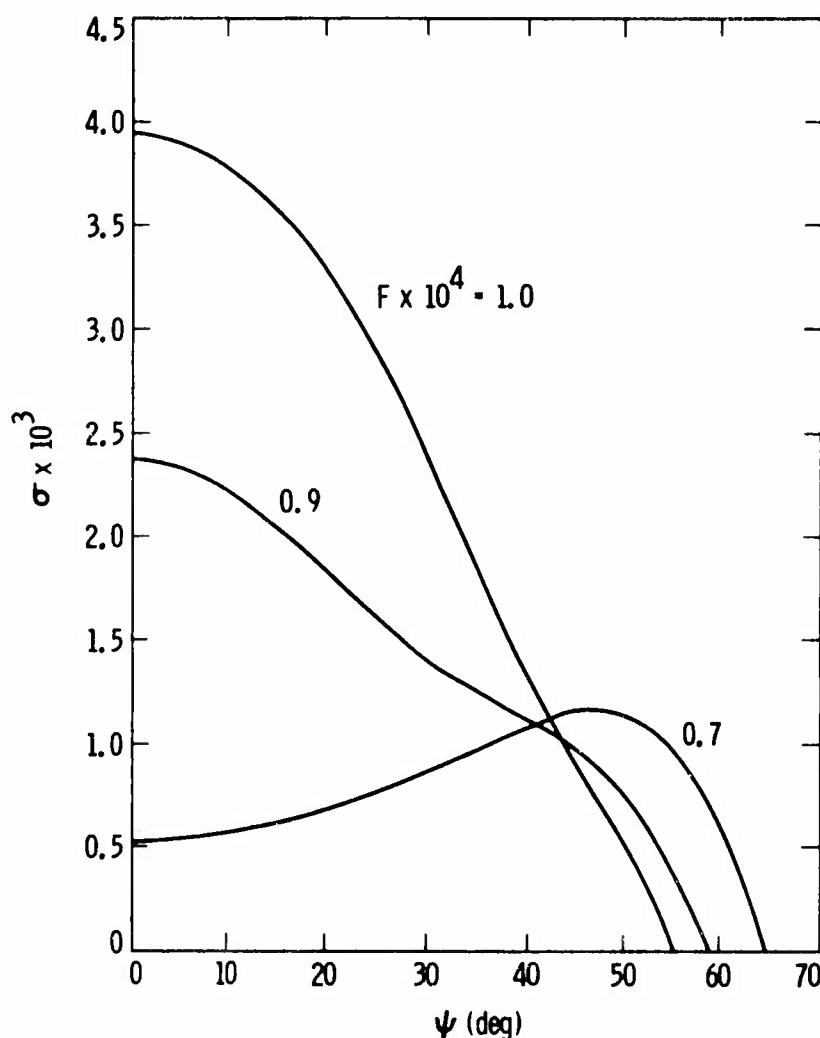


Figure 9. Effect of wave angle on spatial amplification rate of three frequencies at  $R = 1732$ .  $M_e = 6.8$ , cone;  $T_0^* = 728^\circ K$  ( $1310^\circ R$ ).

respect to spanwise wavenumber, as a function of frequency. This is done at  $R = 1245$  in Fig. 10. With the criterion for a first-mode wave that there is a local maximum in the amplification rate at some  $\psi > 0^\circ$ , the highest frequency with first-mode character is  $F = 1.1 \times 10^{-4}$ , where the maximum occurs at  $\psi = 39^\circ$ . All higher frequencies have their maximum amplification rates at  $\psi = 0^\circ$ . Consequently, the wave angle of  $\sigma_{max}$  does not increase gradually from zero as  $F$  decreases, but jumps suddenly from zero to a value near  $40^\circ$ .

When single normal modes are used at each Reynolds number to represent the propagation of a constant-frequency oblique wave, a condition has to be imposed on the spanwise wavenumber component. The condition adopted here is taken from kinematic wave theory, and is that the wavenumber vector is irrotational. This is actually a continuity condition on the phase. For a wave in a 2D planar boundary layer with  $\alpha$  and  $\beta$  independent of  $z$ , it reduces to the condition that the dimensional spanwise wavenumber component is constant.

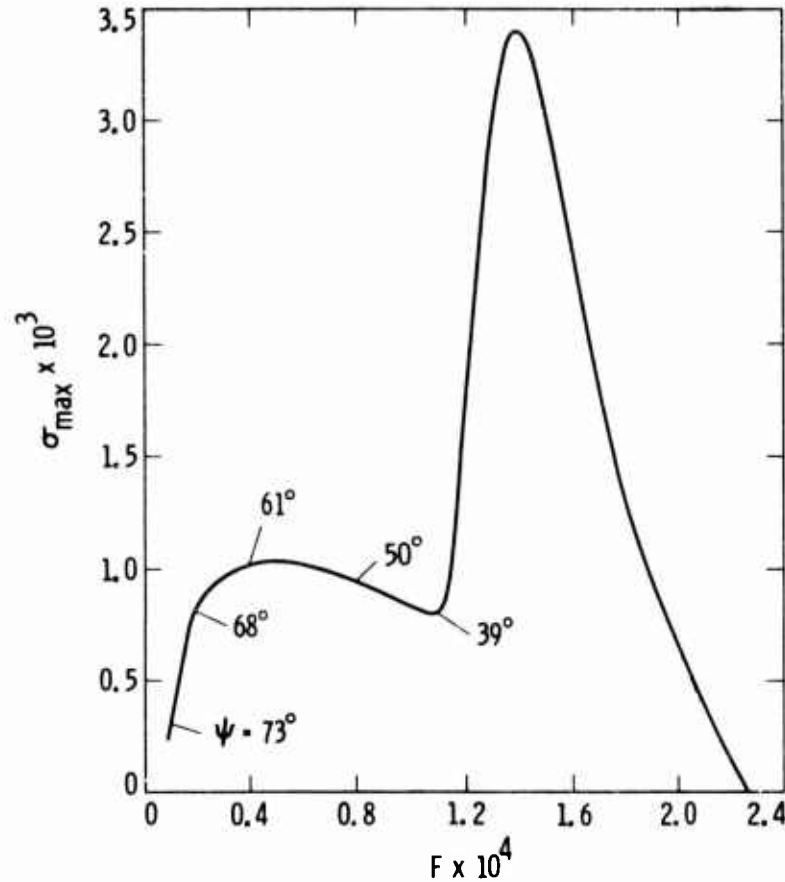


Figure 10. Maximum spatial amplification rate vs frequency at  $R = 1245$ ; wave angle noted where different from zero.  $M_e = 6.8$ , cone;  $T_0^* = 728^\circ K$  ( $1310^\circ R$ ).

In dimensionless terms, the condition is that  $\beta/R$  is a constant. The effect of this condition is that the wave angle increases slightly as the wave propagates downstream. There is also in general a similar condition on the imaginary part of  $\beta$ , but in this report only normal modes with  $\beta$  real are used. For a cone, the irrotationality condition is that the azimuthal wavenumber component  $\beta_\theta$  is constant. In the wavenumber definitions used here,  $\beta_\theta = \beta R \sin \phi_c$ , where  $\phi_c$  is the cone half angle, and the condition is that  $\beta R$  is constant. The effect of this condition is that an oblique wave straightens out as it propagates downstream, and the wave angle  $\psi$  tends towards zero as  $R$  becomes large.

As an example of oblique-wave propagation on a cone, the stability characteristics of four waves with  $F = 1.0 \times 10^{-4}$  are given in Figs. 11-13 and compared with a 2D wave of the same frequency. As this frequency has first-mode character up to about  $R = 1400$  for a 2D wave, it is of interest whether the increased amplification rates of the oblique waves in the first-mode region can outweigh the decreased amplification rates in the second-mode region and result in larger  $N$  factors than the 2D wave. In any case, the decrease in the wave angle because of the condition  $\beta R = \text{const.}$ , means that eventually any oblique wave grows (or damps) as a 2D wave with only an increment or decrement in the  $N$  factor to betray its origin as an oblique wave.

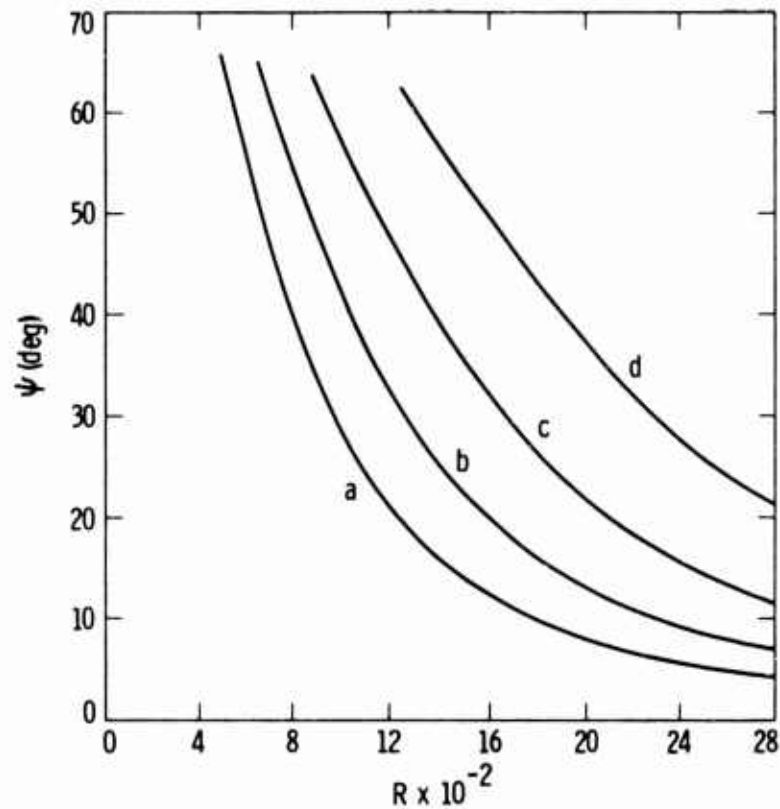


Figure 11. Wave angle vs Reynolds number for four oblique waves;  $F = 1.0 \times 10^{-4}$  (a)  $\beta R = 59.83$ , (b)  $\beta R = 98.92$ , (c)  $\beta R = 170.8$ , (d)  $\beta R = 319.5$ .  $M_e = 6.8$ , cone;  $T_0^* = 728^\circ K$  ( $1310^\circ R$ ).

An oblique wave on a cone is characterized by the value of  $\beta R$ . The four waves examined here have the following values of  $\beta R$ : (a) 59.83; (b) 98.92; (c) 170.8; and (d) 319.5. Figure 11 gives the variation of wave angle with  $R$ . These waves cannot all be started at the same  $R$  in the calculations because of the above mentioned numerical difficulty in the stability codes. For any frequency and Reynolds number, the radius of convergence of the eigenvalue search procedure decreases with increasing  $\psi$ . As a result there is a limiting wave angle beyond which eigenvalues cannot be found. This limit becomes smaller as  $R$  increases for a given  $F$ , or as  $F$  increases for a given  $R$ . Thus the starting angles in Fig. 11 are about the largest that can be used. In Fig. 12 the amplification rates of the four waves are compared to a 2D wave. Wave 'a' initially has oblique first-mode behavior, but for  $R > 1400$  it is close to a 2D second-mode wave with only slightly smaller amplification rates. Waves 'b' and 'c' have larger first-mode amplification rates than wave 'a', but correspondingly smaller second-mode amplification rates. Wave 'd' has first-mode behavior only for the largest wave angles, and its second-mode amplification is much reduced compared to wave 'c'.

The  $N$  factors of the four waves are compared to a 2D wave in Fig. 13. Wave 'b' has the largest  $N$  factors in the first-mode region, and in the second-mode region has a slightly larger  $N$  factor (not shown) than the 2D wave. Wave 'a' has lower  $N$  factors in the first-mode region than wave 'b', but in the second-mode region it is the wave with the largest  $N$  factors.

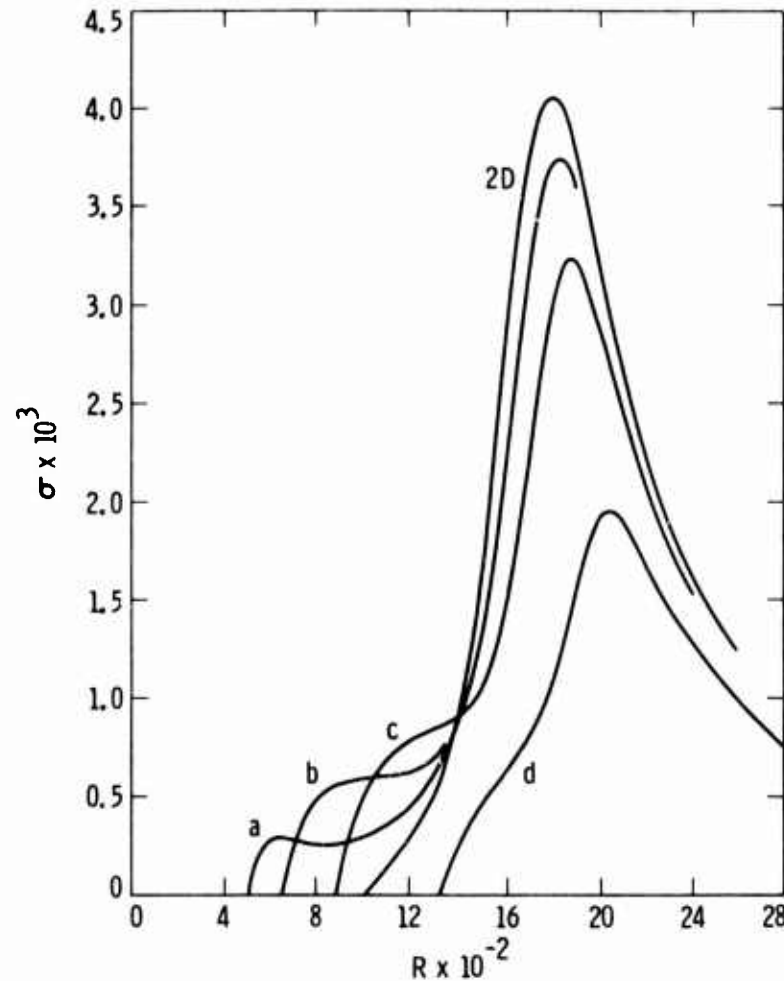


Figure 12. Spatial amplification rate vs Reynolds number for four oblique waves and comparison with 2D wave;  $F = 1.0 \times 10^{-4}$ : (a)  $\beta R = 59.83$ , (b)  $\beta R = 98.92$ , (c)  $\beta R = 170.8$ , (d)  $\beta R = 319.5$ ;  $M_e = 6.8$ , cone;  $T_0^* = 728^\circ K (1310^\circ R)$ .

The other two waves have reduced  $N$  factors in the second-mode region compared to a 2D wave. Note that even in the optimum case, the increment in  $N$  over a 2D wave is quite small, and that locally the wave grows almost as a 2D wave. Consequently, pre-transition linear wave growth at  $M_e = 6.8$  in a cone boundary layer is dominated by 2D second-mode waves.

## 2. COMPARISON WITH EXPERIMENT

In this Section, some comparisons will be made between the stability calculations and the measurements of STDS. First, some comments are in order regarding these comparisons and what may be expected of them. The experiments measure power spectra in the boundary layer of whatever disturbances happen to be present. There is no way to control the origin of the disturbances, or to identify the fluctuations as instability waves, or to determine the spanwise wavenumber spectrum of what is measured. Amplification rates in the STDS experiment were obtained from the spectra at the  $y$  locations of the peak wide-band response,



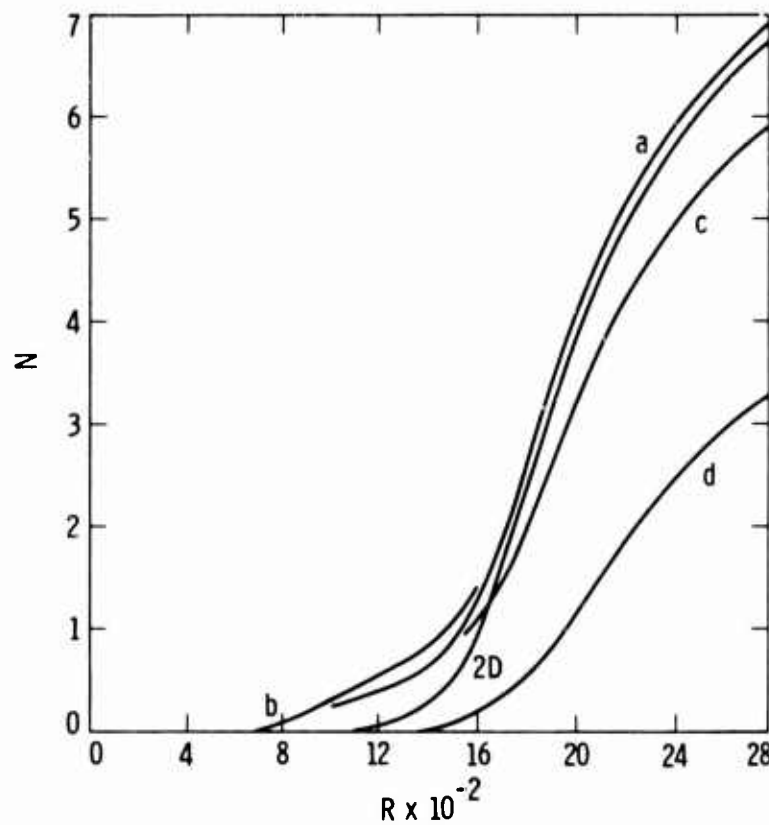


Figure 13.  $N$  factor vs Reynolds number for four oblique waves and comparison with 2D wave;  $F = 1.0 \times 10^{-4}$ : (a)  $\beta R = 59.83$ , (b)  $\beta R = 98.92$ , (c)  $\beta R = 170.8$ , (d)  $\beta R = 319.5$ ;  $M_e = 6.8$ , cone;  $T_c^* = 728^\circ K (1310^\circ R)$ .

which are not necessarily the locations of the peaks of the individual frequency components. As to the calculations, they are of particular normal modes and two points must be kept in mind. First, the "amplitude"  $A$  in the definition of  $N$  does not correspond to the physical wave amplitude, which, unlike  $A$ , is dependent on both the physical quantity being measured and the  $y$  measurement station in the boundary layer. However, it is convenient to think of  $A$  as an actual amplitude measured in some consistent manner, such as was done in the experiments where the maximum amplitude point in the boundary layer, either wide or narrow-band, was used. Second, although the normal modes have been selected to represent possible wave motion, they are definitely not the response of the boundary layer to any specific input such as a point source, much less to whatever the actual input is in the wind tunnel. Consequently, while normal modes with frequencies near the calculated most-unstable frequency can be expected to be present in the experiment, the measured amplitude ratios and amplification rates cannot be expected to agree with normal-mode calculations of these quantities.

In Fig. 14, the calculated maximum spatial amplification rate at  $R = 1732$ , where the maximum is with respect to spanwise wavenumber, is given as a function of the dimensionless frequency,  $F$ , and compared with measurements at  $R = 1728$ . The numerical relation between  $F$  and  $f^*$  (in khz) is  $F = 1.16 \times 10^{-6} f^*$  for  $Re_\infty / ft = 1.0 \times 10^6$  ( $Re_e / ft = 1.42 \times 10^6$ ).

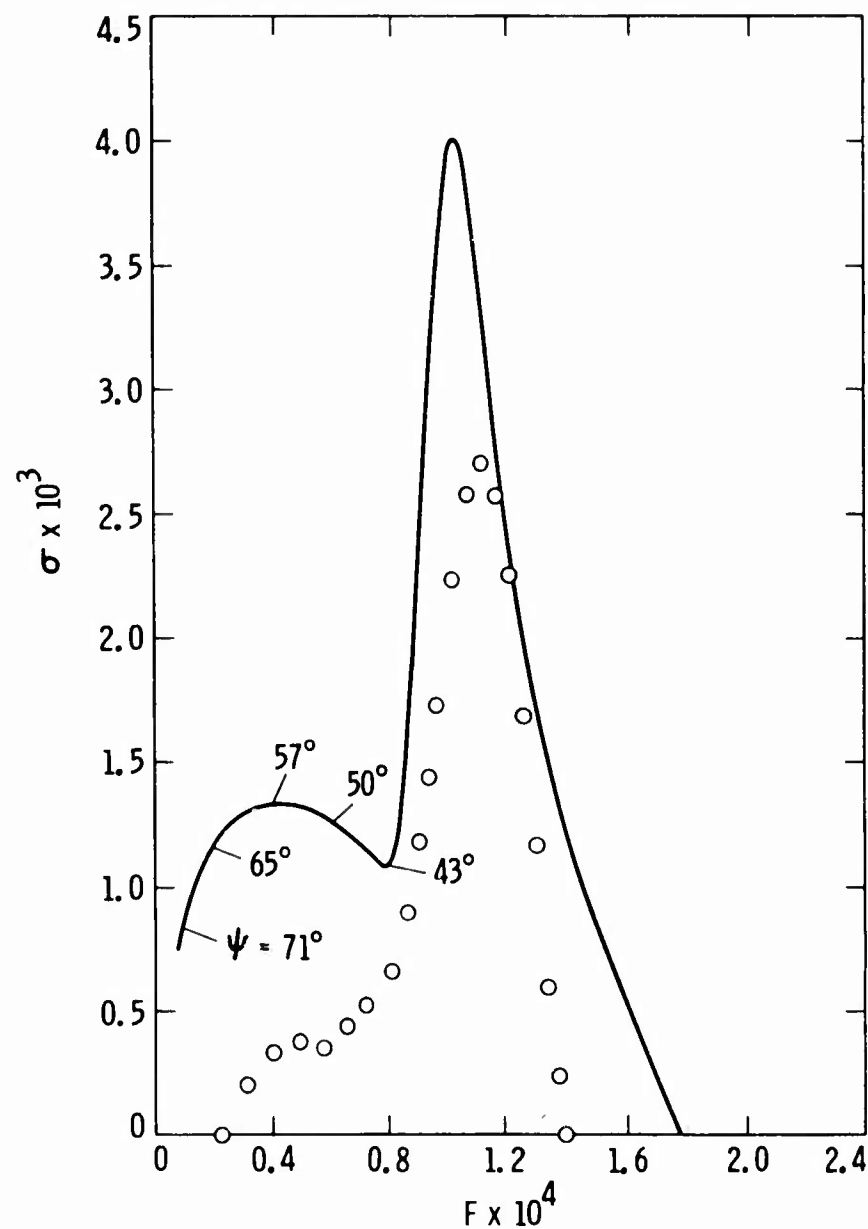


Figure 14. Spatial amplification rate vs frequency at  $R = 1731$ : —, calculated maximum with respect to  $\beta$  (wave angles noted where different from zero); o — experimental points from Stetson *et al.* (Ref. 16),  $Re_\infty/ft = 1.0 \times 10^6$ ,  $M_e = 6.8$ , cone;  $T_0^* = 728^\circ K$  ( $1310^\circ R$ ).

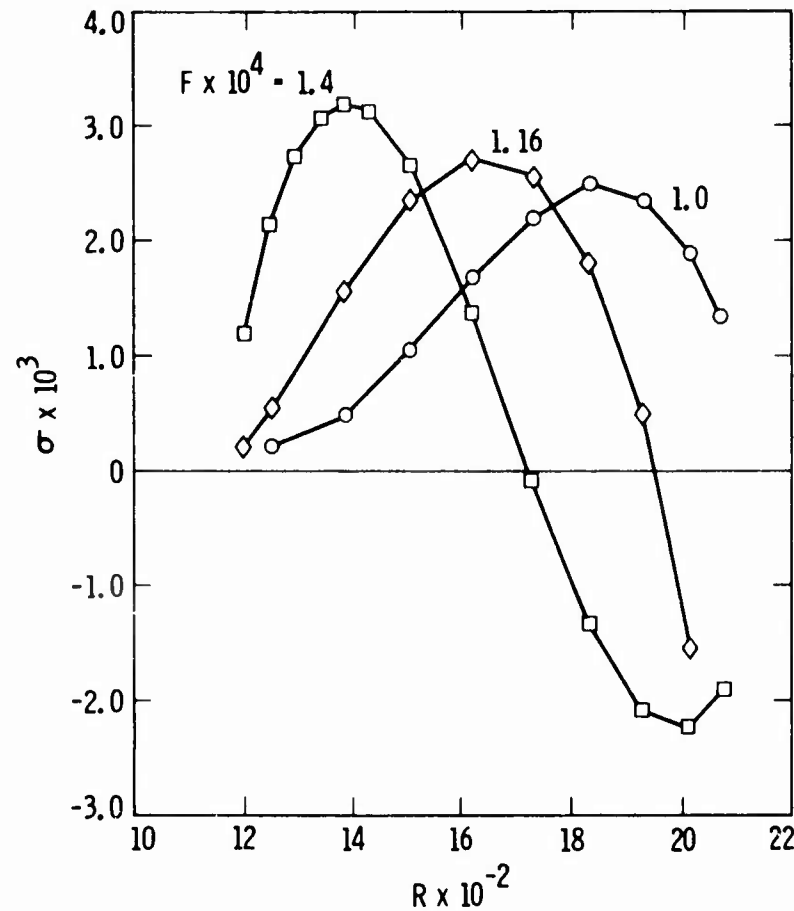


Figure 15. Experimental spatial amplification rate vs Reynolds number for three frequencies from Stetson *et al.* (Ref. 16),  $Re_\infty / ft = 1.0 \times 10^6$ ,  $M_e = 6.8$ , cone;  $T_0^* = 728^\circ K$  ( $1310^\circ R$ ).

Although the experimental amplification rates are shown as data points for clarity, they are taken from the tabulated results of the STDS procedure of fitting a fourth-degree polynomial to the hot-wire amplitude measurements. These results were provided to the author by Stetson (Ref. 33). In Fig. 14, the measured frequency of the maximum amplification rate is within 10% of the calculated value. The measured second-mode amplification rates are for the most part considerably smaller than the theoretical, but differences in this quantity, as mentioned in the previous paragraph, are not surprising. The measured upper-branch neutral frequency is only about 78% of the calculated value. A notable difference between the calculations and measurements is the low values of the measured first-mode amplification rates. Indeed, the measured amplification rates are in much better agreement with calculated 2D first-mode amplification rates (see Fig. 3) than with the oblique-wave amplification rates of the figure. This difference could merely be a reflection of some of the factors mentioned above, or it could possibly be an indication that instability waves are produced so far upstream that the oblique waves of the spectrum have been mostly straightened out by the time that  $R = 1728$  is reached.

In Fig. 15, experimental amplification rates for three frequencies are given as a function

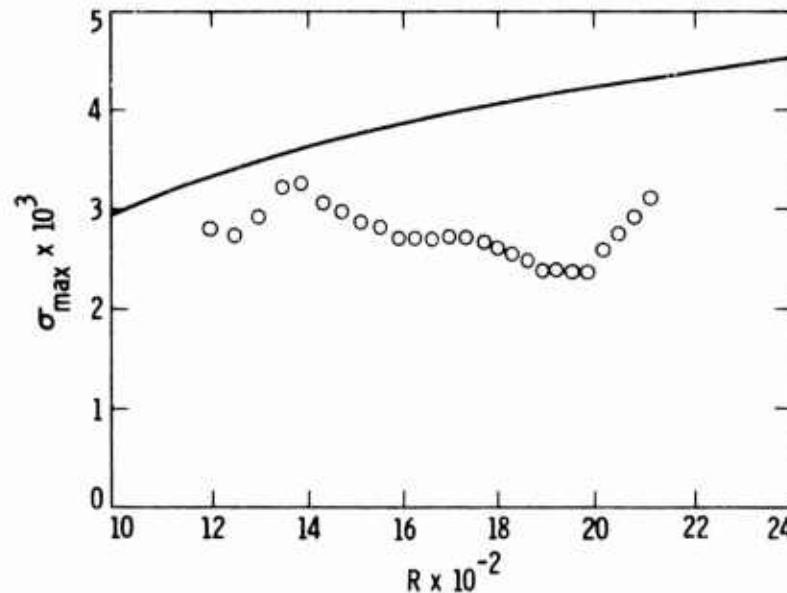


Figure 16. Comparison of calculated maximum 2D spatial amplification rate vs Reynolds number with experimental values from Stetson *et al.* (Ref. 16),  $Re_{\infty}/ft = 1.0 \times 10^6$ ,  $M_e = 6.8$ , cone;  $T_0 = 728^\circ K$  ( $1310^\circ R$ ).

of Reynolds number. What are plotted as data points are again taken from the tabulated data of Ref. 33. Comparison with Fig. 4 shows that there are major discrepancies with the calculations. The experimental peak amplification rate of  $F = 1.4 \times 10^{-4}$  occurs at  $R = 1380$ , well downstream of the calculated peak at  $R = 1250$ . However, this difference decreases with decreasing  $F$ , and the calculated and measured peaks of  $F = 1.0 \times 10^{-4}$  are close together. The measured upper-branch neutral points are at lower Reynolds numbers than the calculated neutral points, and this difference increases with decreasing  $F$ . The slowly decreasing parts of the  $\sigma$  vs  $R$  curves of Fig. 4 do not exist in the experiment.

A striking discrepancy between Figs. 4 and 15 is in the behavior of the maximum amplification rate,  $\sigma_{\max}$ , as a function of  $R$ . Figure 16 compares the calculated  $\sigma_{\max}$ , with the tabulated values of Ref. 33. Not only are the measured values substantially smaller than the calculated, but the calculated  $\sigma_{\max}$  increases with increasing  $R$ , as in all stability calculations for self-similar boundary layers, while the STDS values decrease about 30% with increasing  $R$  for  $1400 < R < 2000$ . The frequencies,  $F_m$ , that correspond to  $\sigma_{\max}$ , are given in Fig. 17. The experimental frequencies differ by as much as 15% from the calculated frequencies at the lower Reynolds numbers, but as  $R$  increases they approach the calculated frequencies more closely.

In Fig. 18, the calculated 2D  $N$  factor for  $F = 1.20 \times 10^{-4}$  is compared with  $N = \ln(A/A_1)$ , the logarithm of an experimental amplitude ratio for  $f^* = 102$  kHz determined from the faired amplitude curve given in Fig. 15 of STDS. The relative vertical positions of the two curves are without meaning, as the experimental reference amplitude  $A_1$  is not the theoretical  $A_0$ , but comparison of the slopes show that this particular frequency grows more slowly in the experiment than in theory. Perhaps the most significant difference is that the measured maximum amplitude occurs at an  $R$  far below the calculated upper-branch neutral point.

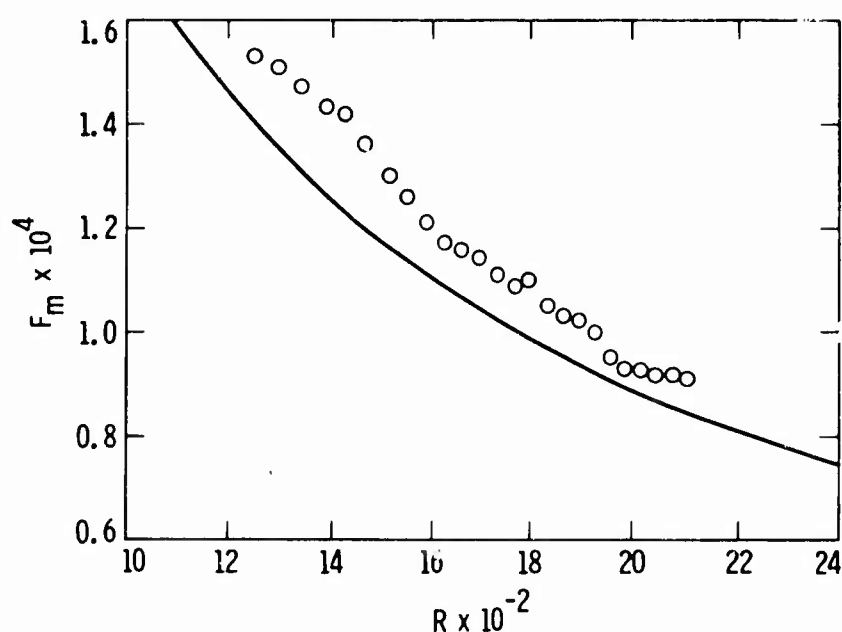


Figure 17. Comparison of calculated frequency of maximum 2D spatial amplification rate with experimental values from Stetson *et al.* (Ref. 16),  $Re_{\infty}/ft = 1.0 \times 10^6$ ,  $M_e = 6.8$ , cone;  $T_0^* = 728^\circ K$  ( $1310^\circ R$ ).

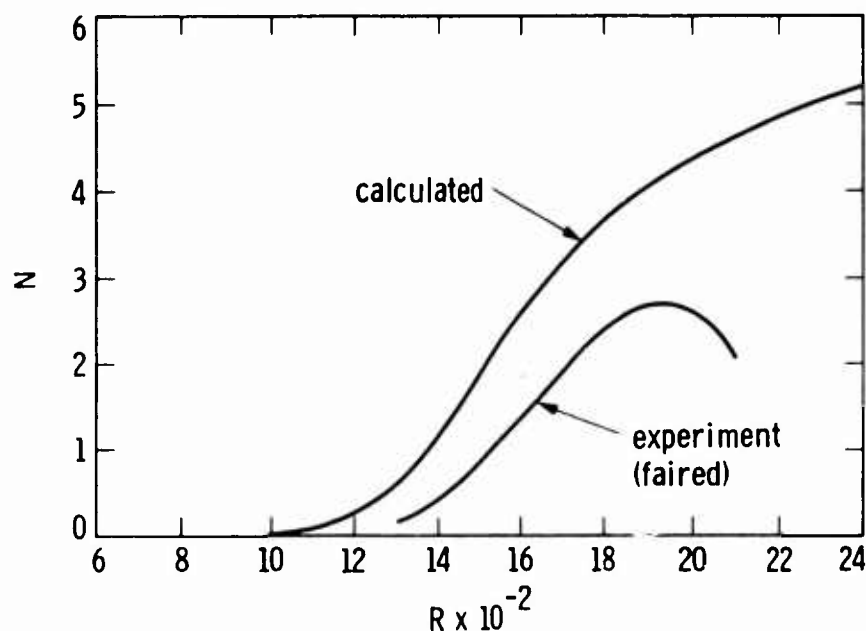


Figure 18. Comparison of calculated 2D  $N$  factor vs Reynolds number with faired amplitude-growth curve from Fig. 15 of Stetson *et al.* (Ref. 16),  $Re_{\infty}/ft = 1.0 \times 10^6$ ,  $M_e = 6.8$ , cone;  $F = 1.2 \times 10^{-4}$ ,  $T_0^* = 728^\circ K$  ( $1310^\circ R$ ).

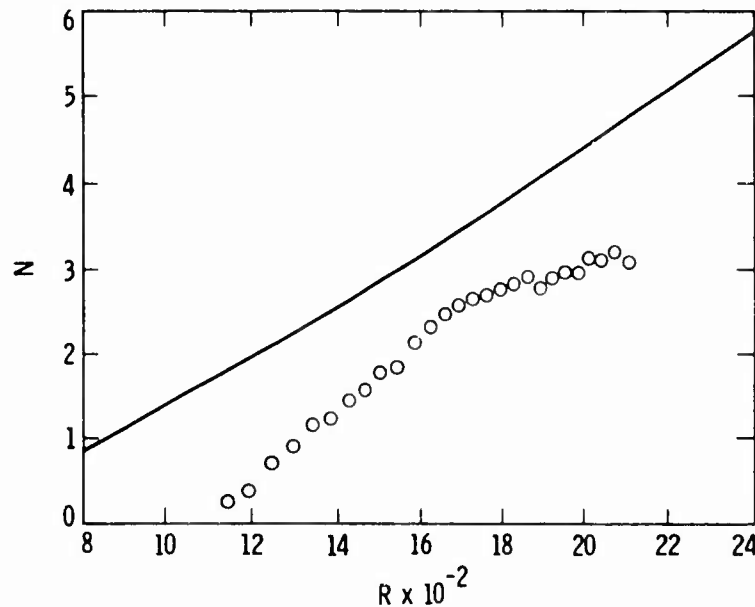


Figure 19. Comparison of calculated 2D  $N$ -factor envelope curve with experimental peak amplitudes: —, calculated 2D  $N$ -factor envelope curve; o —  $\ln(A_{max}/A_1)$  from Fig. D-2 of Stetson *et al.* (Ref. 18),  $Re_\infty/ft = 1.0 \times 10^6$ ,  $M_e = 6.8$ , cone;  $T_0^* = 728^\circ K$  ( $1310^\circ R$ ).

The early leveling off of the growth, which is consistent with Fig. 15, could possibly be related to the start of transition, or at least to the end of the linear region. The start-of-transition Reynolds number estimated by STDS in Ref. 18 from considerations of spectral broadening is about  $R_e = 4.6 \times 10^6$  ( $R = 2150$ ).

In Fig. 19, the calculated 2D  $N$ -factor envelope curve is compared with  $\ln(A_{max}/A_1)$ , the maximum experimental  $N$  factor at each  $R$  as given in Fig. D-2 of Ref. 18. The quantity  $A_{max}$  is the rms spectral amplitude peak at each Reynolds number. The logarithm of this amplitude referenced to  $A_1$ , the extrapolated  $A_{max}$  at  $R = 1094$ , is what is plotted in Fig. 19 as the experimental data ( $A_1$  is slightly different from the  $A_1$  of Fig. 18). As in Fig. 18, the magnitudes of the calculated and experimental  $N$  factors are not comparable because  $A_0$  and  $A_1$  are different quantities. However, the curves do show relative amplitude growth provided that  $A_0$  is independent of frequency as in  $A_1$ . It is seen that initially the measured maximum disturbance growth is faster than calculated, but at about  $R = 1700$  a break occurs in the slope and the subsequent growth is slower. This break is about where  $\sigma_{max}$  of the corresponding  $F$  starts to decrease with increasing  $R$  in Fig. 16. It is also downstream of where the high-frequency unstable zone was first noted by STDS (see Ref. 18, Fig. 6) at  $R = 1420$ , but is close to the Reynolds number where the frequency bandwidth of this zone is a maximum.

The frequencies,  $F_{env}$ , that correspond to the amplitudes of Fig. 19 are shown in Fig. 20. Because of the graphical determination of the envelope curve, the Reynolds numbers at which the calculated frequencies are tangent to the envelope curve are not as accurate as other calculated quantities. The experimental frequencies are the frequencies of the peaks of the first bumps in the faired amplitude spectra given in Fig. 17 of STDS. The agreement between

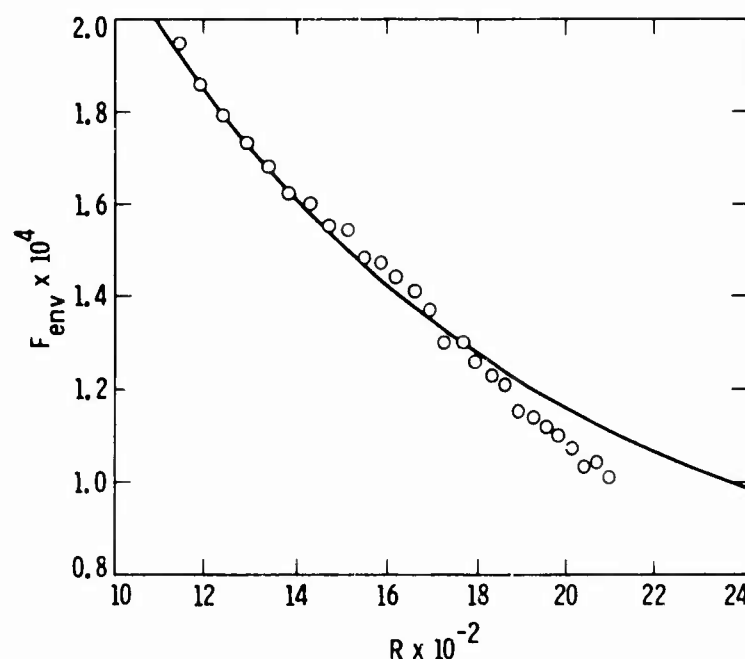


Figure 20. Comparison of calculated and experimental frequencies of peak amplitude: —, calculated 2D envelope-curve frequencies; o — measured frequencies of peak amplitude from Stetson *et al.* (Ref. 16),  $Re_{\infty}/ft = 1.0 \times 10^6$ ,  $M_e = 6.8$ , cone;  $T_0^* = 728^\circ K$  ( $1310^\circ R$ ).

theory and experiment is remarkable. The experimental values follow the theoretical curve within 3% up to about  $R = 1860$ ; at higher Reynolds numbers the difference increases to 9%. The fact that the measurements agree less well with the calculations at the higher Reynolds numbers is the opposite of the situation with the frequency of the peak amplification rate.

As already mentioned in Section III, STDS interpreted all spectral amplitude changes as an indication of instability. This procedure seems to be justified when there is a definite bump in the spectrum, but for certain frequencies there are large amplification rates indicated even though no bump appears in the spectrum. It is of some interest to locate the prominent first spectral bumps of Fig. 17 in Ref. 16 in the  $F, R$  plane. Figure 21 shows the upper and lower boundaries of the bump as determined from the large-size plots of Ref. 33. Also shown in the figure are the calculated 2D upper and lower neutral boundaries, as well as the calculated boundary between the first and second modes. The latter is not clearly defined; it has been taken as the frequency where the 2D amplification rate starts to increase rapidly. Note that the upper frequency limit of the spectral bump falls on the calculated upper neutral boundary, and the lower limit falls on the lower boundary of the second-mode region. As the calculated boundaries are determined from amplification rates, not amplitudes, no particular explanation can be offered for this result, which may be coincidental, but it does serve to further define the spectral bump as a second-mode phenomenon. Note that the upper bump limit also corresponds to a neutral boundary in STDS, but there it is the *lower* neutral boundary of a *second* unstable region.

A major difference between the stability calculations and the three stability experiments is that there is nothing in the linear theory to correspond to the second unstable region

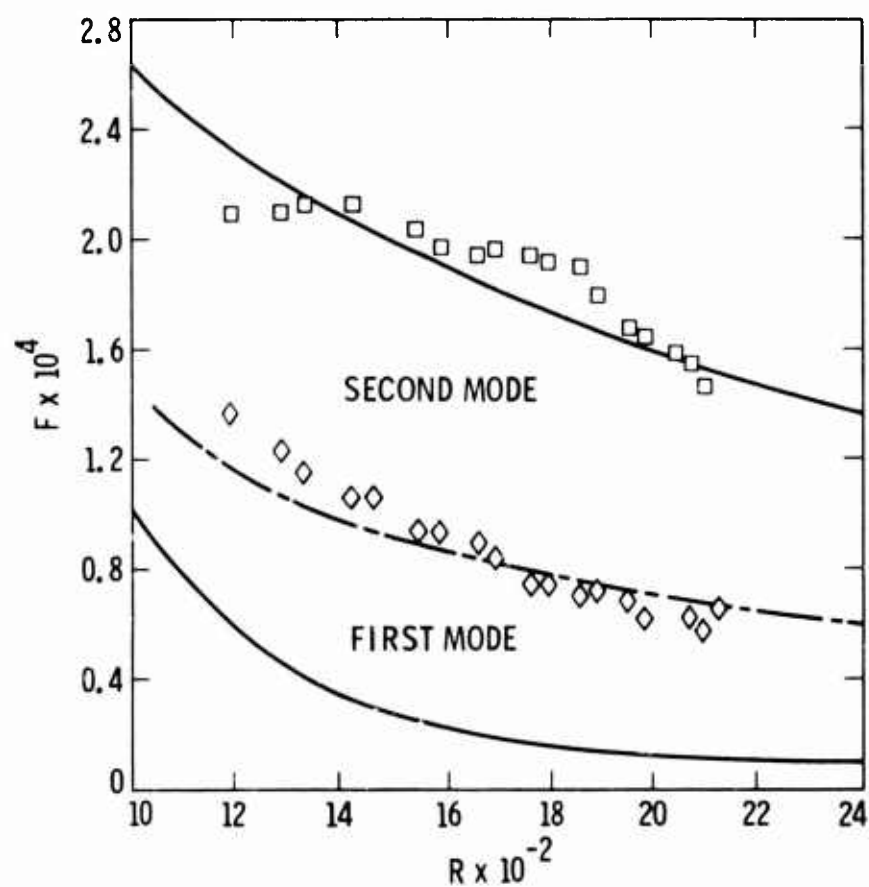


Figure 21. Calculated neutral boundaries, —; calculated boundary between first and second mode, — · —;  $\square$ , measured upper limit of first spectral bump (Fig. 17 of Ref. 16);  $\diamond$ , measured lower limit of first spectral bump (same reference).  $M_e = 6.8$ , cone;  $T_0^* = 728^\circ K$  ( $1310^\circ R$ ); experimental points,  $Re_\infty / ft = 1.0 \times 10^6$ .



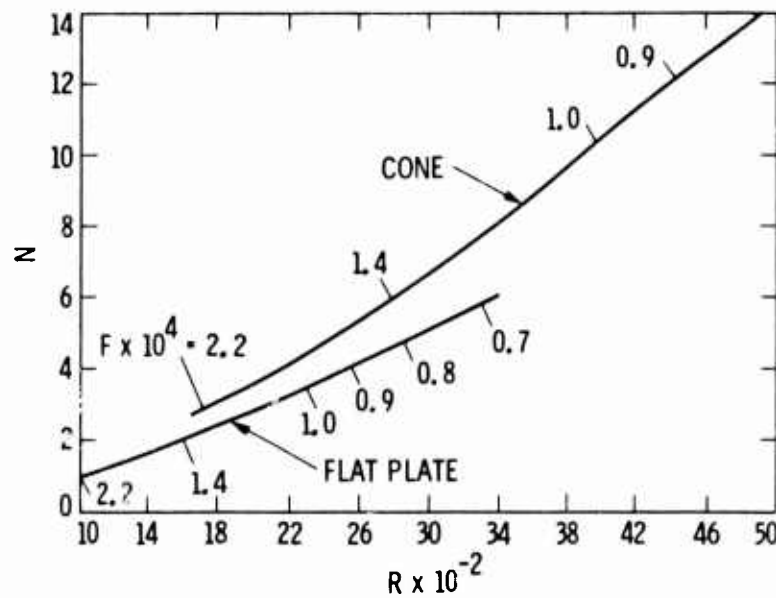


Figure 22. Comparison of 2D cone and flat-plate  $N$ -factor envelope curves.  $M_e = 4.5$ ,  $T_0^* = 311^\circ K$  ( $560^\circ R$ ).

that appears in the experiments above the second-mode region. In the STDS experiment, this instability eventually shows up as a second spectral bump at about  $R = 1700$  with a peak frequency not far from twice the peak frequency of the first bump. For  $R > 1900$ , the peak frequency of the second bump is quite close to twice the frequency of the first bump. According to the linearized stability equations used in this report, the frequencies of the second unstable region are all damped, and the damped region that separates the two unstable regions in the experiments is unstable.

### 3. CONE VS FLAT PLATE

As a final topic, some results of normal-mode stability calculations for flat plates and cones are presented in order to compare amplitude growth curves. Such curves may be used to indicate what one might expect the difference in transition Reynolds numbers to be in these two cases based solely on linear stability theory. Figure 22 shows the 2D envelope curves for a cone and flat plate at  $M_e = 4.5$  and a stagnation temperature of  $311^\circ K$  ( $560^\circ R$ ). At this Mach number, the first and second-mode unstable regions are separated by a damped region (Mack, Ref. 1). The waves with  $F \times 10^4 < 1.4$  pass through all three regions. The  $N$ -factor reference amplitude  $A_0$  is the amplitude on the first-mode lower branch as long as the first-mode total amplification exceeds the inter-region damping, which is the usual case. Otherwise, it is the amplitude on the second-mode lower branch. Only the flat-plate envelope curve was calculated; the curve for the cone was obtained by the Battin-Lin transformation rule (Ref. 26). It is evident that 2D cone  $N$  factors are greater than 2D flat-plate  $N$  factors except at very low Reynolds numbers, and at the same Reynolds number the cone frequencies are larger than for a flat plate.

In the first-mode region, oblique waves are the most unstable. Figure 23 compares the

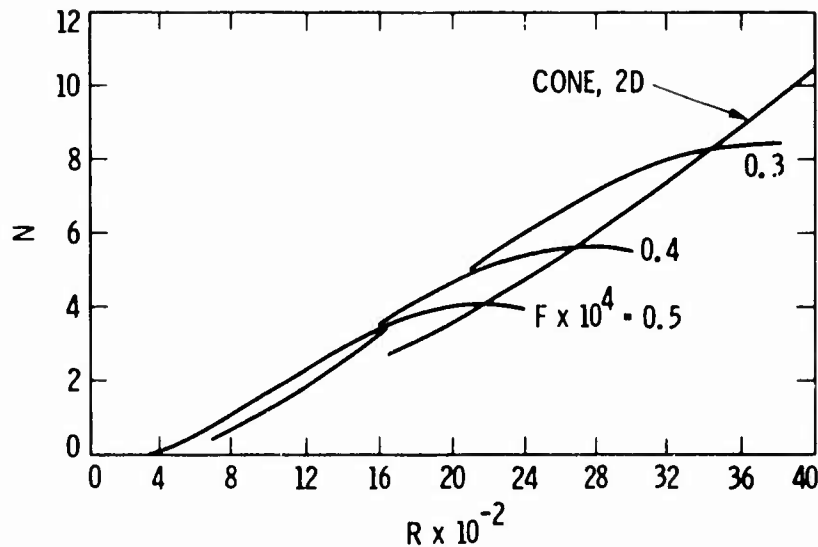


Figure 23. Comparison of 2D cone  $N$ -factor envelope curve with curves of  $N$  factor vs Reynolds number for three flat-plate oblique waves with  $\psi = 55^\circ$  at critical Reynolds number.  $M_e = 4.5$ ,  $T_0^* = 311^\circ K$  ( $560^\circ R$ ).

2D cone envelope curve with flat-plate  $N$  factors for three low-frequency oblique waves which have wave angles approximately equal to  $55^\circ$  at their lower-branch neutral points. The irrotationality condition,  $\beta/R = \text{const.}$ , has been applied in calculating the flat-plate  $N$  factors. An envelope curve has not been drawn, because these waves are not necessarily those with the maximum growth. However, the results demonstrate that not only do these first-mode oblique waves have appreciably larger  $N$  factors on a flat plate than 2D waves, but they also have somewhat greater growth than 2D waves on a cone. The frequencies of these waves on a flat plate are much lower than the frequencies on the 2D cone envelope curve at the same Reynolds numbers.

Oblique first-mode waves are also more unstable than 2D first-mode waves on a cone. Only actual calculation can establish whether this greater instability of low-frequency waves results in greater growth than the 2D, mostly second-mode, waves of greatest growth in view of the decrease in wave angle that occurs on the cone because of the irrotationality condition. Figure 24 compares the 2D cone envelope curve with the results of calculations for two first-mode oblique waves with  $\beta R = 201.7$ . This value of  $\beta R$  has not been optimized, but it is evident that on a cone, just as on a flat plate, low-frequency first-mode oblique waves can have greater growth than higher frequency 2D waves. A comparison with Fig. 23 shows that, at least for  $R > 1800$ , a cone still has slightly greater  $N$  factors than a flat plate even when oblique waves are considered. Also the frequencies of the oblique waves of maximum growth are comparable on a cone and flat plate. Thus at this Mach number, normal-mode stability calculations would not lead one to expect an appreciable difference between the transition Reynolds numbers on a cone and flat plate, and certainly offer no support for a higher transition Reynolds number on a cone.

The 2D cone and envelope curves at  $M_e = 5.8$  are given in Fig. 25 for a stagnation temperature of  $386^\circ K$  ( $696^\circ R$ ). A comparison with Fig. 22 shows that both boundary layers are more unstable to 2D waves at this Mach number than at  $M_e = 4.5$ . Indeed the cone

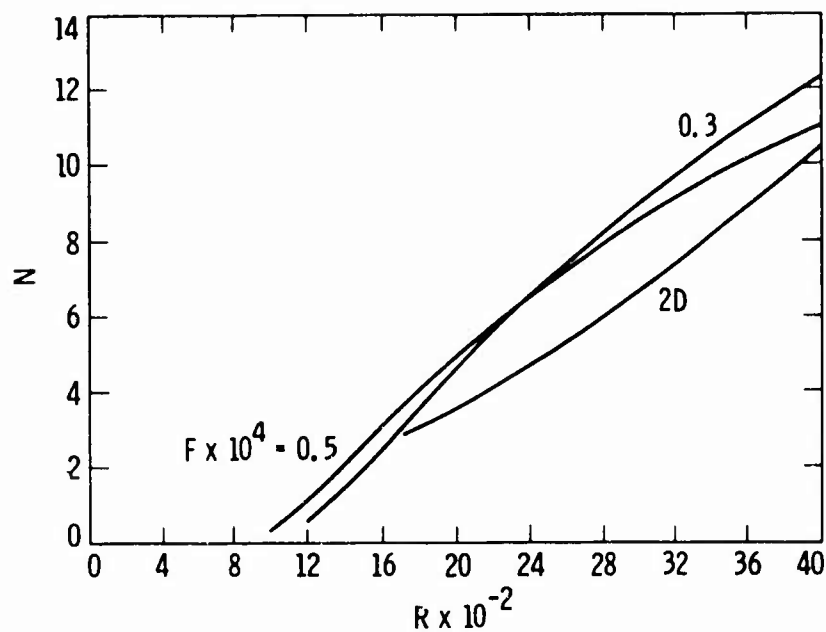


Figure 24. Comparison of 2D cone  $N$  factor envelope curve with curves of  $N$  factor vs Reynolds number for two oblique waves on a cone with  $\beta R = 201.7$ .  $M_e = 4.5$ ,  $T_0^* = 311^\circ K$  ( $560^\circ R$ ).

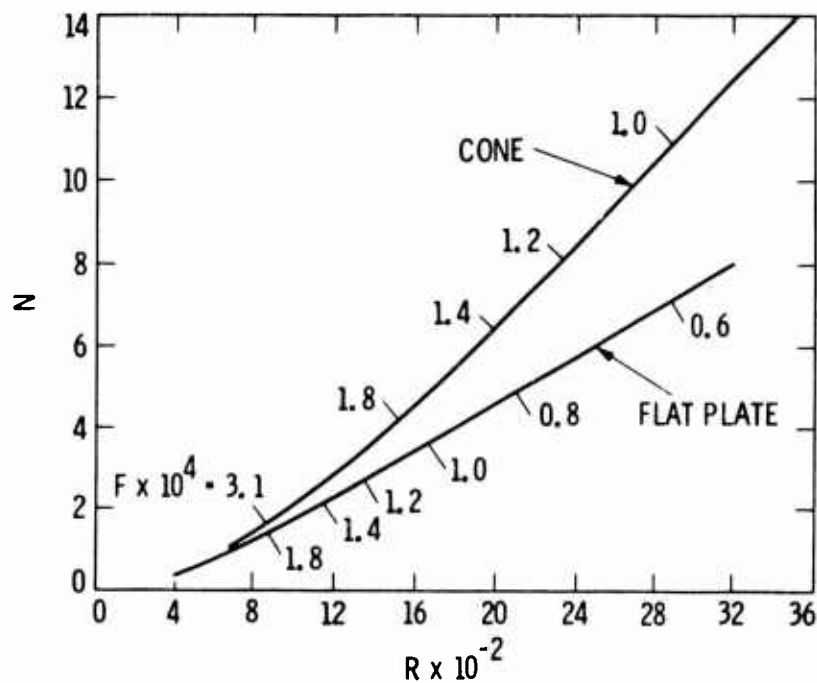


Figure 25. Comparison of 2D cone and flat-plate  $N$ -factor envelope curves.  $M_e = 5.8$ ,  $T_0^* = 386^\circ K$  ( $696^\circ R$ ).

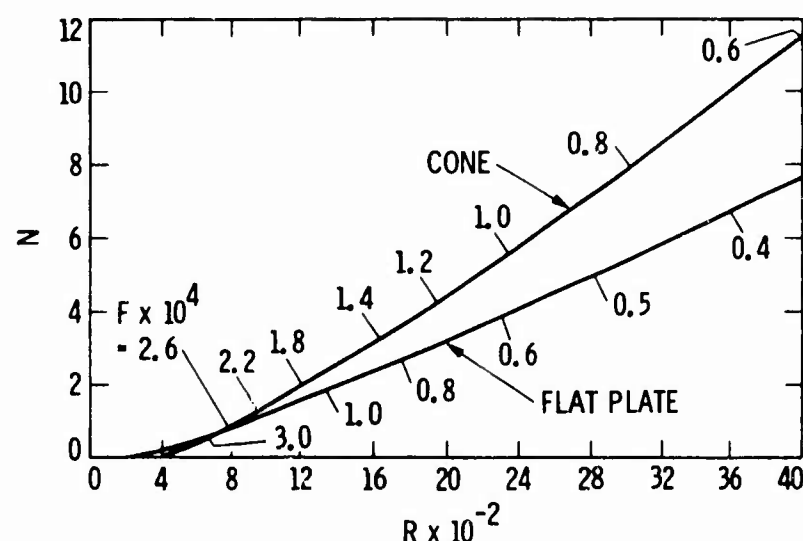


Figure 26. Comparison of 2D cone and flat-plate  $N$ -factor envelope curves.  $M_e = 6.8$ ,  $T_0^* = 728^\circ K$  ( $1310^\circ R$ ).

envelope curve of Fig. 25 has greater growth than any of the growth curves at  $M_e = 4.5$ . Also Fig. 25 shows that, just as at  $M_e = 4.5$ , the maximum 2D wave growth on a cone is greater than on a flat plate. No  $N$  factors for oblique waves have been calculated at  $M_e = 5.8$ , but as the Mach number increases in the hypersonic region, 2D second-mode waves become of more relative importance than first-mode oblique waves.

Finally, in Fig. 26 a 2D cone envelope curve at  $M_e = 6.8$  and a stagnation temperature of  $728^\circ K$  ( $1310^\circ R$ ) that covers a wider Reynolds number range than in Fig. 6 is compared to a 2D flat-plate envelope curve. Again the cone  $N$  factors are greater than the flat-plate  $N$  factors everywhere except for  $R < 740$ . The frequencies along the cone envelope curve are about 65-70% higher than those at the same Reynolds numbers on the flat-plate curve. Note that the stabilizing effect of Mach number in the hypersonic speed range is starting to assert itself and that the  $N$  factors in Fig. 26 are less than in Fig. 25. A number of calculations with oblique waves of different frequencies were carried out at this Mach number for both the cone and flat plate, and in no case could an  $N$  factor greater than given in Fig. 26 be found except for the small increment already noted in Fig. 13. Thus, at this Mach number, as at  $M_e = 4.5$  and  $5.8$ , there is no support from normal-mode linear stability calculations for cones having a transition Reynolds number higher than, or even the same, as on a flat plate.

## SECTION VI CONCLUSIONS

The numerical calculations and comparisons with the experiment of STDS have led to some conclusions and a number of uncertainties concerning the stability of the flow over sharp cones at zero angle of attack. These are summarized below.

a. The stagnation temperature is an important parameter for insulated-wall boundary layers. An increase of  $T_0^*$  from  $512^\circ K$  ( $922^\circ R$ ) to  $728^\circ K$  ( $1310^\circ R$ ) has been shown to lead to a significant stabilization of the boundary layer.

b. Locally planar flow has been assumed in the stability analysis with the neglect of all  $1/r^*$  terms in the stability equations, where  $r^*$  is the cone radius. Although the boundary-layer thickness is small compared to the cone radius for a  $7^\circ$  half-angle cone, the importance of the neglected terms should be checked by actual calculation. The effect of including transverse curvature in the mean flow only was investigated and found to be small.

c. The calculations show that the only significant instability at  $M_e = 6.8$  comes from 2D waves of the second mode. The experiment of STDS confirms this by failing to show any appreciable response at first-mode frequencies, and by the strong response in the second-mode frequency range. The excellent agreement between the calculated frequencies of the most-amplified normal modes and the measured frequencies of the amplitude peaks demonstrates that these normal modes are indeed present in the actual flow and are responsible for the maximum growth.

d. There are important disagreements between the amplification rates determined from the spectra of the naturally occurring disturbances in the boundary layer and the amplification rates of the normal modes used in the calculations both as to frequency and magnitude. There are at least two reasons why this is so. First, the interpretation of all changes in spectral amplitude as due to instability may not be correct. The boundary-layer response to the input disturbances, which is determined by receptivity, is not limited to instability waves. Second, the part of the response that consists of instability waves is not limited to the individual spatial normal modes of the calculations. It can be expected that an entire frequency and spanwise-wavenumber spectrum of phase-related normal modes will be excited, and it is the superposition of these normal modes that determines the actual wave motion. If a dominant normal mode exists, it is likely to be not a spatial wave, but a mode with complex  $\omega$  and  $\beta$ .

e. When the frequency limits of the primary spectral amplitude bump of STDS are plotted in  $F, R$  space, the lower limit falls in the calculated boundary between the first and second modes, and the upper limit on the upper-branch (second-mode) neutral boundary. No explanation can be offered as to why boundaries determined from measured amplitudes should agree with boundaries calculated from amplification rates.

f. Apparently the only way to verify the spatial normal-mode calculations, other than measuring a 2D spectrum with complete phase information and performing a Fourier decomposition, is by introducing controlled disturbances into the boundary layer that excite only the assumed normal modes.

g. The theoretical problem that is of more interest than normal-mode calculations is the determination of the wave motion produced by the same input as is responsible for the instability waves in the experiments. A simpler problem is to calculate the response to a source, such as a harmonic or pulsed point source, that can be duplicated experimentally.

h. A major unsettled question is the origin of the unstable frequency band that lies above the second-mode frequencies in the stability experiments. This unstable band, which is separated from the second-mode unstable band by a damped region, does not exist in linear stability theory. Indeed, its *lower* neutral boundary is close to the calculated *upper* neutral boundary of the second mode.

i. No criterion is known by which to judge where the processes that follow linear instability, such as nonlinear wave interactions or secondary instability, start in a hypersonic boundary layer. In a hypersonic boundary layer, the velocity fluctuations are small and the density fluctuations large. As the second unstable region does not exist in the present linear calculations it is probably the result of nonlinearity. The frequency band where it occurs suggests a first harmonic of the second mode.

j. The existence of a surface temperature gradient in the STDS experiment should not have had an important effect on the measurements. Second-mode instability is not strongly affected by small amounts of heat transfer. This was confirmed by calculations (not reported in the preceding text) with the ratio of surface temperature to recovery temperature equal to 0.95. No significant effects were found.

k. The comparisons between cone and flat-plate  $N$  factors for  $M_e \geq 4.5$  offer no support for the experimental finding of a greater transition Reynolds number for a cone than for a flat plate. At  $M_e = 4.5$ , the maximum cone  $N$  factors are at least as large as for a flat plate except at low  $R$  where there is not much growth, and at  $M_e = 5.8$  and  $6.8$ , the cone  $N$  factors are greater than for a flat plate. However, it cannot be emphasized too strongly that there is an enormous gap between normal-mode  $N$  factors and transition. The disturbances present in the wind tunnel, their receptivity into the boundary layer, the actual forms of the instability waves that are generated, nonlinear processes and secondary instabilities, and the whole final breakdown to turbulent flow, all influence the transition Reynolds number. What can be concluded is that one has to look elsewhere than to normal-mode calculations based on the planar, quasi-parallel, linear stability equations to explain the measured differences between the end-of-transition Reynolds numbers on cones and flat plates.

## APPENDIX

### COEFFICIENT MATRIX OF COMPRESSIBLE STABILITY EQUATIONS

There are 30 non-zero elements of the coefficient matrix  $a_{ij}(y)$  of Eq. (13). The  $Z_1$  equation has only one non-zero coefficient:

$$a_{12} = 1 \quad (A1)$$

The  $Z_2$  equation has six non-zero coefficients:

$$\begin{aligned} a_{21} &= \frac{iR}{\mu T}(\alpha U + \beta W - \omega) + \alpha^2 + \beta^2, \\ a_{22} &= -\frac{1}{\mu} \frac{d\mu}{dT} DT, \\ a_{23} &= \frac{R}{\mu T}(\alpha DU + \beta DW) - i(\alpha^2 + \beta^2) \frac{1}{\mu} \frac{d\mu}{dT} DT \\ &\quad - i \frac{1}{3}(1 + 2d)(\alpha^2 + \beta^2) \frac{DT}{T}, \\ a_{24} &= \frac{iR}{\mu}(\alpha^2 + \beta^2) - \frac{1}{3}(1 + 2d)(\alpha^2 + \beta^2) \gamma M_e^2(\alpha U + \beta W - \omega), \\ a_{25} &= \frac{1}{3}(1 + 2d)(\alpha^2 + \beta^2) \frac{1}{T}(\alpha U + \beta W - \omega) \\ &\quad - \frac{1}{\mu} \frac{d\mu}{dT}(\alpha D^2 U + \beta D^2 W) - \frac{i}{\mu} \frac{d^2 \mu}{dT^2} DT(\alpha DU + \beta DW), \\ a_{26} &= -\frac{1}{\mu} \frac{d\mu}{dT}(\alpha DU + \beta DW). \end{aligned} \quad (A2)$$

The  $Z_3$  equation has four non-zero coefficients:

$$\begin{aligned} a_{31} &= -i, \\ a_{33} &= \frac{DT}{T}, \\ a_{34} &= -i \gamma M_e^2(\alpha U + \beta W - \omega), \\ a_{35} &= \frac{i}{T}(\alpha U + \beta W - \omega). \end{aligned} \quad (A3)$$

The  $Z_4$  equation is the only one that requires a lengthy manipulation to derive. With

$$E = \frac{R}{\mu} + i\frac{2}{3}(2+d)\gamma M_e^2(\alpha U + \beta W - \omega), \quad (\text{A4})$$

the six non-zero coefficients are:

$$\begin{aligned} a_{41} &= -\frac{i}{E} \left[ \frac{2}{\mu} \frac{d\mu}{dT} DT + \frac{2}{3}(2+d) \frac{1}{T} DT \right], \\ a_{42} &= -\frac{i}{E}, \\ a_{43} &= \frac{1}{E} \left[ -(\alpha^2 + \beta^2) + \frac{2}{3}(2+d) \frac{1}{\mu T} \frac{d\mu}{dT} (DT)^2 \right. \\ &\quad \left. + \frac{2}{3}(2+d) \frac{D^2 T}{T} - \frac{iR}{\mu T} (\alpha U + \beta W - \omega) \right], \\ a_{44} &= -\frac{i}{E} \frac{2}{3}(2+d)\gamma M_e^2 \left[ \frac{1}{\mu} \frac{d\mu}{dT} DT (\alpha U + \beta W - \omega) \right. \\ &\quad \left. + \alpha DU + \beta DW + \frac{1}{T} DT (\alpha U + \beta W + \omega) \right], \\ a_{45} &= \frac{i}{E} \left\{ \frac{1}{\mu} \frac{d\mu}{dT} (\alpha DU + \beta DW) + \frac{2}{3}(2+d) \right. \\ &\quad \left. \times \left[ \frac{1}{\mu T} \frac{d\mu}{dT} DT (\alpha U + \beta W - \omega) + \frac{1}{T} (\alpha DU + \beta DW) \right] \right\}, \\ a_{46} &= \frac{i}{E} \frac{2}{3}(2+d)(\alpha U + \beta W - \omega). \end{aligned} \quad (\text{A5})$$

The  $Z_5$  equation has only one non-zero coefficient:

$$a_{56} = 1, \quad (\text{A6})$$

The  $Z_6$  equation has six non-zero coefficients:

$$\begin{aligned} a_{62} &= -2\sigma(\gamma - 1)M_e^2(\alpha DU + \beta DW)(\alpha^2 + \beta^2)^{-1}, \\ a_{63} &= \frac{R\sigma}{\mu T} DT - i2\sigma(\gamma - 1)M_e^2(\alpha DU + \beta DW), \\ a_{64} &= -\frac{iR\sigma}{\mu}(\gamma - 1)M_e^2(\alpha U + \beta W - \omega), \\ a_{65} &= \frac{iR\sigma}{\mu T}(\alpha U + \beta W - \omega) + \alpha^2 + \beta^2 - \frac{1}{\kappa} \frac{d\kappa}{dT} D^2 T \\ &\quad - \frac{1}{\kappa} \frac{d^2 \kappa}{dT^2} (DT)^2 - \sigma(\gamma - 1)M_e^2 \frac{1}{\mu} \frac{d\mu}{dT} [(DU)^2 + (DW)^2], \end{aligned} \quad (\text{A7})$$



$$a_{66} = -\frac{2}{\kappa} \frac{d\kappa}{dt} DT,$$

$$a_{68} = -2\sigma(\gamma - 1)M_e^2(\alpha DW - \beta DU)(\alpha^2 + \beta^2)^{-1}.$$

The  $Z_7$  equation has only one non-zero coefficient:

$$a_{78} = 1. \quad (A8)$$

The  $Z_8$  equation has five non-zero coefficients:

$$\begin{aligned} a_{83} &= \frac{R}{\mu T}(\alpha DW - \beta DU), \\ a_{85} &= -\frac{1}{\mu} \frac{d\mu}{dt}(\alpha D^2 W - \beta D^2 U) - \frac{1}{\mu} \frac{d^2 \mu}{dT^2} DT(\alpha DW - \beta DU), \\ a_{86} &= -\frac{1}{\mu} \frac{d\mu}{dT}(\alpha DW - \beta DU), \\ a_{87} &= \frac{iR}{\mu T}(\alpha U + \beta W - \omega) + \alpha^2 + \beta^2, \\ a_{88} &= -\frac{1}{\mu} \frac{d\mu}{dT} DT. \end{aligned} \quad (A9)$$

In these equations, the ratio of the second to the first viscosity coefficient

$$d = \lambda/\mu \quad (A10)$$

is taken to be a constant and equal to 1.2 (Stokes' assumption corresponds to  $\lambda = 0$ ).

In the numerical computations, the viscosity coefficient is given by the Sutherland law plus a linear variation with temperature for  $T^*$  greater than the Sutherland constant. In cgs units,

$$\begin{aligned} \mu^* \times 10^5 &= 1.458 T^{*3/2} / (T^* + 110.4), & T^* \geq 110.4^\circ K, \\ &= 0.0693873 T^*, & T^* < 110.4^\circ K. \end{aligned} \quad (A11)$$

The thermal conductivity coefficient in cgs units is given by a formula of Keyes (Ref. 34):

$$\kappa^* = 0.6325 T^{*1/2} \left[ 1 + (245.4/T^*) \times 10^{-12/T^*} \right]^{-1}. \quad (A12)$$

The Prandtl number  $\sigma = c_p^* \mu^* / \kappa^*$  is computed as a function of temperature from  $\mu^*(T^*)$ ,  $\kappa^*(T^*)$  and a constant specific heat of  $c_p^* = 0.24$ .

## REFERENCES

1. Mack, L.M., "Boundary-Layer Stability Theory", Internal Document No. 900-277, Rev. A, Jet Propulsion Laboratory, Pasadena, CA, 1969.
2. Mack, L.M., "Boundary-Layer Linear Stability Theory," *Special Course on Stability and Transition of Laminar Flow*, edited by R. Michel, AGARD Report No. 709, pp.3-1 to 3-81, 1984.
3. Malik, M.R., "Instability and Transition in Supersonic Boundary Layers," *Laminar-Turbulent Boundary Layers*, edited by E.M. Uram and H.E. Weber, Proceedings of Energy Resources Technology Conference, New Orleans, LA, Feb. 12-16, 1984.
4. Sternberg, J., "A Free-flight Investigation of the Possibility of High Reynolds Number Supersonic Laminar Boundary Layers," *Journal of the Aeronautical Sciences*, Vol. 19, 1952, pp. 721-733.
5. Laufer, J. and Marte, J.E., "Results and Critical Discussion of Transition Reynolds Number Measurements on Insulated Cones and Flat Plates in Supersonic Wind Tunnels," Report No. 20-96, Jet Propulsion Laboratory, Pasadena, CA, 1955.
6. Van Driest, E.R. and Boison, J.C., "Experiments on Boundary-Layer Transition at Supersonic Speeds," *Journal of the Aeronautical Sciences*, 1957, Vol. 21, pp. 885-899.
7. Potter, J.L. and Whitfield, J.D., "Boundary-Layer Transition Under Hypersonic Conditions," AGARDograph 97, Part 3, 1965, pp. 1-61, 1965 (also AEDC TR-65-99, May 1964).
8. Pate, S.R., "Measurements and Correlations of Transition Reynolds Numbers on Sharp Slender Cones at High Speed," *AIAA Journal*, Vol. 9, 1971, pp. 1082-1090.
9. Dougherty, N.S., Jr. and Steinle, F.W., Jr., "Transition Reynolds Number Comparisons in Several Major Transonic Tunnels," AIAA Paper No. 74-627, 1974.
10. Dougherty, N.S., Jr. and Fisher, D.F., "Boundary Layer Transition on a 10 deg Cone: Wind Tunnel/Flight Data Correlations," AIAA Paper 80-0154 (see also NASA TP 1971, 1982).
11. Potter, J.L., "Boundary-Layer Transition on Supersonic Cones in an Aeroballistic Range," *AIAA Journal*, Vol. 13, 1975, pp. 270-277.
12. Sheetz, N.W., Jr., "Ballistic Range Boundary-Layer Transition Measurements on Cones at Hypersonic Speeds", *Proceedings of the Navy-NASA-LTV Symposium on Viscous Drag Reduction*, edited by J.R. Spangler and C.S. Wells, Jr., Plenum Press, 1969, pp. 53-83.
13. Reda, D.C., "Boundary-Layer Transition Experiments on Sharp, Slender Cones in Supersonic Free Flight," *AIAA Journal*, Vol. 17, 1979, pp. 803-810.

14. Kendall, J.M., "Wind Tunnel Experiments Relating to Supersonic and Hypersonic Boundary-Layer Transition," *AIAA Journal*, Vol. 13, 1975, pp. 240-299.
15. Demetriades, A., "Laminar Boundary Layer Stability Measurements at Mach 7 Including Wall Temperature Effects," AFOSR-TR-77-1311, Nov. 1977.
16. Stetson, K.F., Thompson, E.R., Donaldson, J.C. and Siler, L.G., "Laminar Boundary Layer Stability Experiments on a Cone at Mach 8. Part 1. Sharp Cone, AIAA Paper 83-1761, 1983.
17. Stetson, K.F., Thompson, E.R., Donaldson, J.C. and Siler, L.G., "Laminar Boundary Layer Stability Experiments on a Cone at Mach 8. Part 2. Blunt Cone," AIAA Paper 83-1761, 1984.
18. Stetson, K.F., Thompson, E.R., Donaldson, J.C., and Siler, L.G., "Laminar Boundary Layer Stability Experiments on a Cone at Mach 8. Part 3. Sharp Cone at Angle of Attack," AIAA Paper 85-0492, 1985.
19. Brinich, P.F. and Sands, N., "Effect of Bluntness on Transition for a Cone and a Hollow Cylinder at Mach 3.1," NACA TN No. 3979, 1957.
20. Stetson, K.F. and Rushton, G.H., "Shock Tunnel Investigation of Boundary Layer Transition at  $M = 5.5$ ," *AIAA Journal*, Vol. 5, 1967, pp. 899-906.
21. Stainback, P.C., "Effect of Unit Reynolds Number, Nose Bluntness, Angle of Attack and Roughness on Transition of a 5 deg Half-Angle Cone at Mach 8," NASA TN D-4961, 1969.
22. Softley, E.J., "Boundary Layer Transition of Hypersonic Blunt, Slender Cones," AIAA Paper 69-705, June 1969.
23. Muir, J.F. and Trujillo, A.A., "Experimental Investigation of the Effects of Nose Bluntness, Free-stream Unit Reynolds Number and Angle of Attack on Cone Boundary Layer Transition at a Mach number of 6," AIAA Paper 72-216, 1972.
24. Stetson, K.F., "Hypersonic Boundary Layer Transition Experiments," AFWAL-TR-80-3062, Oct. 1980.
25. Khan, M.M.S. and Reshotko, E., "Stability of the Laminar Boundary Layer on a Blunted Plate in Supersonic Flow," Department of Mechanical and Aerospace Engineering, Case Western Reserve University, FTAS TR-79-142 (see also M.M.S. Khan, Ph.D. Dissertation, 1979).
26. Battin, R.H. and Lin, C.C., "On the Stability of the Boundary Layer Over a Cone," *Journal of the Aeronautical Sciences*, Vol. 17, 1950, p. 453.
27. Tetervin, A.N., "A Discussion of Cone and Flat-plate Reynolds Numbers for Equal Ratios of the Laminar Shear to the Shear Caused by Small Velocity Fluctuations in a Laminar Boundary Layer," NACA TM No. 4078, 1957.

28. Whitfield, J.D. and Iannuzzi, F.A., "Experiments on Roughness Effects on Cone Boundary-Layer Transition up to Mach 16," *AIAA Journal*, Vol. 7, 1969, pp. 465-470.
29. Mangler, W., Zusammenhang zwischen ebenen und rotationsymmetrischen Grenzschichten in kompressiblen Flüssigkeiten, *ZAMM*, Vol. 28, 1948, pp. 97-103.
30. Gentry, A.E. and Wazzan, A.R., "The Transition Analysis Program System." Vol II-Program Formulation and Listing, Report No. MDC J7255/02, McDonnell Douglas Corp., Long Beach, CA, June 1976.
31. Cebeci T. and Smith, A.M.O., *Analysis of Turbulent Boundary Layers*, Academic Press, NY, 1974.
32. Mack, L.M., "Computation of the Stability of the Laminar Boundary Layer," *Methods of Computational Physics*, edited by B. Alder, S. Fernbach and M. Rotenberg, Vol. 4, Academic Press, NY, 1965, pp. 247-299.
33. Stetson, K.F., Tabulated and plotted data of Ref. 16, private communication.
34. Keyes, F.G., "A Summary of Viscosity and Heat-conduction Data for He, A, H<sub>2</sub>, O<sub>2</sub>, CO, CO<sub>2</sub>, H<sub>2</sub>O, and Air," *Transactions of the ASME*, Vol. 73, 1951, pp. 589-596.